PERSPECTIVE

Check for updates

Metal–organic framework based bifunctional oxygen electrocatalysts for rechargeable zinc–air batteries: current progress and prospects

Yanqiang Li, [ID] †*[a] Ming Cui,†[a] Zehao Yin,[a] Siru Chen[d] and Tingli Ma [ID] *[bc]

Zinc–air batteries (ZABs) are regarded as ideal candidates for next-generation energy storage equipment due to their high energy density, non-toxicity, high safety, and environmental friendliness. However, the slow oxygen reduction reaction (ORR) and oxygen evolution reaction (OER) kinetics on the air cathode limit their efficiency and the development of highly efficient, low cost and stable bifunctional electrocatalysts is still challenging. Metal–Organic Framework (MOF) based bifunctional oxygen electrocatalysts have been demonstrated as promising alternative catalysts due to the regular structure, tunable chemistry, high specific surface area, and simple and easy preparation of MOFs, and great progress has been made in this area. Herein, we summarize the latest research progress of MOF-based bifunctional oxygen electrocatalysts for ZABs, including pristine MOFs, derivatives of MOFs and MOF composites. The effects of the catalysts' composites, morphologies, specific surface areas and active sites on catalytic performances are specifically addressed to reveal the underlying mechanisms for different catalytic activity of MOF based catalysts. Finally, the main challenges and prospects for developing advanced MOF-based bifunctional electrocatalysts are proposed.

1. Introduction

The depletion of traditional fossil fuels and ever-increasing environmental pollution have prompted great interest in developing advanced energy conversion and storage technologies related to alternative energy sources. Nowadays, the lithium-ion battery is one of the most widely utilized electrochemical energy devices since its successful commercialization in the late 1990s.[1–3] However, the insufficient energy density (<350 W h kg^{-1}), poor safety, and high cost (~\$150 kW^{-1} h^{-1}) of lithium-ion batteries restrict their large-scale application to some extent.[3–6] Although other metal-ion batteries such as sodium-ion batteries have a lower price, the energy density of SIBs is much lower and the stability of SIBs is very poor. Lithium–sulfur batteries with a higher energy density also face the issue of poor stability and safety.[3,7–10] In this regard, metal–air batteries especially Zn–air batteries have received great

attention due to their unique advantages: (i) high energy density: the energy density of ZABs (1086 and 1370 W h kg^{-1}, including oxygen and excluding oxygen) is several times higher than that of lithium-ion batteries;[7,10–13] (ii) suitable working voltage and intrinsic safety: the working voltage of ZABs is appropriately high and will not cause the decomposition of water in the electrolyte;[7,10,14] (iii) low cost (~\$100 kW^{-1} h^{-1}) and a stable discharge profile.

However, during the charge and discharge of rechargeable ZABs, the chemical reaction kinetics of the oxygen reduction reaction (ORR) and oxygen evolution reaction (OER) on the air cathode are very sluggish, resulting in their round-trip energy efficiency usually less than 55–65%.[14,15] At present, the most outstanding electrocatalysts for the ORR and OER are precious metal materials, such as Pt/C for the ORR and RuO$_2$/IrO$_2$ for the OER.[16,17] However, the high costs, low natural reserves, single-reaction catalytic activity, and poor durability of noble metals hampered their widespread application.[18–20] Therefore, it is important and urgent to develop efficient, durable, and low-cost bifunctional electrocatalysts for the ORR and OER.

Metal–organic frameworks (MOFs) are a class of materials with crystalline porous structures and periodic frameworks connected by metal ions and organic ligands through coordinate bonds.[21–23] MOFs have the advantages of high porosity, a large surface area, adjustable compositions and structures, *etc.*[24,25] Recent progress demonstrated the great potential of MOF-based electrocatalysts for ZABs due to the following unique advantages: (i) the large specific surface area of the

[a]*State Key Laboratory of Fine Chemicals, School of Petroleum and Chemical Engineering, Dalian University of Technology, Panjin Campus, Panjin 124221, China. E-mail: yanqiangli@dlut.edu.cn*

[b]*Department of Materials Science and Engineering, China Jiliang University, Hangzhou, 310018, China. E-mail: tinglima123@cjlu.edu.cn*

[c]*Graduate School of Life Science and Systems Engineering, Kyushu Institute of Technology, Kitakyushu, Fukuoka 808-0196, Japan. E-mail: tinglima@life.kyutech.ac.jp*

[d]*Center for Advanced Materials Research, Zhongyuan University of Technology, Zhengzhou, 450007, China. E-mail: siruchen@zut.edu.cn*

† These authors contributed equally to this work.

catalysts can expose more active sites and increase the contact of the catalysts with the electrolyte in ZABs. In addition, the spatial accessibility of the highly ordered topology can further improve the efficiency of the mass transmission process.[26–28] (ii) It is convenient to introduce multiple metallic/nonmetallic heteroatoms as active sites of the catalysts.[29,30] The electronic structure of the catalysts can be readily turned by the various composites in them, thereby reducing the adsorption energy of various intermediates in the ORR/OER process. The synergistic effect between various substances can further promote the improvement of catalytic activity.[31,32] (iii) The catalysts derived from direct pyrolysis of MOFs or MOF composites with other highly conductive substrates can enhance the conductivity of the catalysts, thereby accelerating the electron transfer.[26,33–36] (iv) Heterostructured catalysts can be readily prepared by using MOF composites, which can create abundant interfaces and active sites.[37,38] (v) By rationally designing the structures of MOFs such as the size, porosity, hierarchical structure and distribution of active sites,[39,40] it is possible to obtain electrocatalysts with high catalytic activity and strong stability in the harsh catalytic environment of ZABs (Table 1).

In this review, we systematically summarize the research progress of MOF-based ORR and OER bifunctional electrocatalysts in recent years, and highlight their application in rechargeable ZABs (Fig. 1). The synthesis methods and catalytic mechanisms of various types of MOF-based electrocatalysts are reviewed. The effects of catalysts' structure and composition on their performance are analyzed and the strategies to improve their activity are proposed. Finally, the challenges and prospects for the development of advanced MOF-based electrocatalysts for ZABs are prospected. We hope that this review could give researchers a timely and valuable reference for developing advanced bifunctional catalysts and manufacturing high-performance rechargeable ZABs.

2. Configurations and reaction mechanisms for ZABs, the ORR and the OER

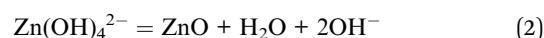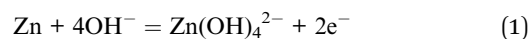### 2.1 Configurations and reaction mechanisms for ZABs

Rechargeable ZABs can be divided into liquid batteries and solid-state batteries according to the electrolyte. The composition of a common liquid ZAB is: zinc anode, separator, concentrated alkaline electrolyte and air cathode, as shown in Fig. 2A. The activity of catalysts for the OER and ORR on the air cathode is one of the most critical factors that determine the performance of ZABs. The zinc anode is usually a pure Zn plate and the electrolyte is usually alkaline media with a high concentration to offer a high ionic conductivity. The most widely adopted electrolyte for aqueous ZABs is 6 M KOH with an ionic conductivity of 620 mS cm^{-1}. In most cases, a low concentration of $Zn(Ac)_2$ or $ZnCl_2$ (0.2 M) is added into the electrolyte to facilitate the reversible conversion of the Zn anode. The air cathode of ZABs is composed of an electrocatalyst, gas diffusion layer and current collector and normally contains hydrophilic and hydrophobic sides. The bifunctional

electrocatalyst contacts with the electrolyte on the hydrophilic side, while the hydrophobic side is a barrier to prevent electrolyte leakage and provides a channel for air entering to react on the surface of catalysts. In addition, the typical configuration of a flexible solid ZAB is shown in Fig. 2B, where the main distinction with a liquid battery is the solid gel electrolyte, which is placed between the zinc anode and the air cathode. The solid gel electrolyte reported is mainly polyvinyl alcohol (PVA) gel with high concentration KOH, which is prepared by adding KOH into PVA solution to form a homogeneous solid gel.

The chemical reactions involved in the charge and discharge processes of ZABs can be summarized as follows:
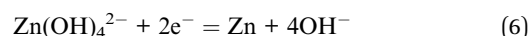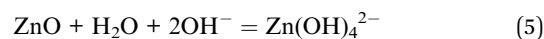
Discharge:

Anode:

$$Zn + 4OH^- = Zn(OH)_4^{2-} + 2e^- \tag{1}$$
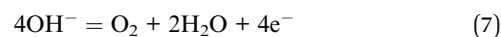
$$Zn(OH)_4^{2-} = ZnO + H_2O + 2OH^- \tag{2}$$

Cathode:

$$O_2 + 2H_2O + 4e^- = 4OH^- \tag{3}$$

Overall reaction:

$$2Zn + O_2 = 2ZnO \tag{4}$$

Charge:

Anode:

$$ZnO + H_2O + 2OH^- = Zn(OH)_4^{2-} \tag{5}$$

$$Zn(OH)_4^{2-} + 2e^- = Zn + 4OH^- \tag{6}$$

Cathode:

$$4OH^- = O_2 + 2H_2O + 4e^- \tag{7}$$

Overall reaction:

$$2ZnO = 2Zn + O_2 \tag{8}$$

The theoretical working voltage of ZABs is 1.65 V.[18,35] However, during the charge and discharge process, there is a large overpotential between the ORR and OER, which will reduce the operating voltage of ZABs to a certain extent (generally less than 1.2 V) and result in low energy round-trip efficiency.[41–43] Therefore, the main function of bifunctional electrocatalysts is to reduce overpotentials of the ORR and OER, and to achieve an efficient and stable catalytic reaction process.

2.2 Reaction mechanisms of the ORR

Generally, according to the different reaction pathways on the catalyst surface, the ORR mechanism can be divided into two types: two-electron pathway and direct four-electron pathway. Due to the production of unstable peroxide and corrosive HO$^-$ species, which will affect the efficiency and lifetime of ZABs, the dual-electron mechanism is not an ideal ORR pathway. In contrast, the four-electron approach with higher efficiency is

Table 1 Summary for the electrocatalytic performance and ZAB performance of the MOF-based bifunctional ORR/OER electrocatalysts reported in recent years

Catalyst	OER performance: E_{10} [V]	ORR performance: $E_{1/2}$ [V]	ΔE [V]	Catalyst loading (mg cm⁻²)	Electrolytes	OCP (V)	Power density (mW cm⁻²)	Specific capacity (mA h g⁻¹)	Voltage gap [V]	Cycling performance	Ref.
Mn/Fe–HIB-MOFs	1.51	0.883	0.672	0.15	6 M KOH + 0.2 M Zn(Ac)₂	1.442	194	750	0.65	3600 cycles (600 h) at 25 mA cm⁻²	59
Co₃HITP₂	1.59	0.80	0.79	4.0	6 M KOH + 0.2 M Zn(Ac)₂	—	164	784	—	500 cycles (80 h) at 5 mA cm⁻²	60
CoNi-MOF/rGO	1.548	—	0.83	—	6 M KOH + 0.2 M ZnCl₂	1.37	97	711	0.96	120 h at 5 mA cm⁻²	61
Pt3.2%@NiNSMOFs	1.528	0.863	0.665	0.1	6 M KOH + 0.2 M ZnCl₂	—	108	—	—	—	62
NCo@CNT-NF700	—	0.861	—	0.5	6 M KOH + 0.2 M Zn(Ac)₂	1.46	220	—	0.80	400 cycles (133 h) at 5 mA cm⁻²	75
C-MOF-C2-900	1.58	0.815	0.765	2.0	6 M KOH + 0.2 M Zn(Ac)₂	1.46	105	768	0.54	360 cycles (120 h) at 2 mA cm⁻²	76
Co-N-CNTs	1.69	0.90	0.79	1.0	6 M KOH + 0.2 M Zn(Ac)₂	1.365	101	—	—	130 cycles (15 h) at 2 mA cm⁻²	77
25% Cu–N/C	—	0.813	—	1.0	6 M KOH	1.40	132	—	—	—	78
3DOM Fe–N–C-900	—	0.875	—	1.0	6 M KOH	1.45	235	768.3	—	—	79
Co-SAs@NC	—	0.82	—	1.75	6 M KOH + 0.2 M ZnCl₂	1.46	105	897.1	0.81	240 cycles (80 h) at 10 mA cm⁻²	80
NC-Co SA	1.59	0.87	0.72	1.56	6 M KOH + 0.2 M Zn(Ac)₂	1.411	20.9	—	0.45	570 cycles (180 h) at 10 mA cm⁻²	81
Fe/OES	—	0.85	—	0.52	6 M KOH + 0.2 M Zn(Ac)₂	1.51	186.8	962.7	—	400 cycles (130 h) at 5 mA cm⁻²	82
CoNi-SAs/NC	1.57	0.76	0.81	1.4	6 M KOH + 0.2 M Zn(Ac)₂	1.45	101.4	750.9	0.82	95 cycles (32 h) at 5 mA cm⁻²	92
CoFe20@CC	1.52	0.86	0.66	0.52	6 M KOH + 0.2 M Zn(Ac)₂	1.50	190.3	787.9	—	400 cycles (130 h) at 5 mA cm⁻²	93
Ni₃Fe/Co–N–C	1.55	0.80	0.75	1.0	6 M KOH + 0.2 M Zn(Ac)₂	1.39	68	—	0.78	80 cycles (65 h) at 10 mA cm⁻²	94
FeCo-IA/NC	—	0.88	—	1.0	6 M KOH + 0.2 M ZnCl₂	1.472	115.6	635.3	0.951	—	95
Cu@Fe–N–C	—	0.892	—	1.0	6 M KOH + 0.2 M Zn(Ac)₂	1.35	92	—	—	—	96
NC-Co₃O₄-90	1.588	0.87	0.718	—	11.25 M KOH + 0.25 M ZnO (flexible ZAB)	1.44	82	387.2	—	50 cycles (1000 min) at 10 mA cm⁻²	109
MnO/Co/PGC	1.537	0.78	0.82	10.0	6 M KOH + 0.2 M Zn(Ac)₂	1.52	172	873	—	350 cycles (117 h) at 10 mA cm⁻²	111
Co/Co₃O₄@PGS	1.58	0.89	0.69	0.9	6 M KOH + 0.2 M Zn(Ac)₂	1.45	118.27	—	0.91	4800 cycles (800 h) at 10 mA cm⁻²	113

Table 1 (*Contd.*)

Catalyst	OER performance: E_{10} [V]	ORR performance: $E_{1/2}$ [V]	ΔE [V]	Catalyst loading (mg cm^{-2})	Electrolytes	OCP (V)	Power density (mW cm^{-2})	Specific capacity (mA h g^{-1})	Voltage gap [V]	Cycling performance	Ref.
Co/Co$_x$S$_y$@SNCF-800	1.536	0.74	0.796	2.0	6 M KOH + 0.2 M Zn(Ac)$_2$	1.37	230	—	0.7	468 cycles (800 h)	117
Co$_9$S$_8$@TDC-900	1.56	0.78	0.78	3.5	6 M KOH + 0.2 M Zn(Ac)$_2$	1.50	101.5	—	1.10	270 cycles (45 h) at 5 mA cm^{-2}	118
NiS$_x$/NMC-1.5	1.57	0.898	0.68	1.0	6 M KOH + 0.2 M Zn(Ac)$_2$	1.53	186	785	0.9	300 cycles (100 h) at 10 mA cm^{-2}	119
CoNiFe–S MNs	1.491	0.78	0.711	0.5	6 M KOH + 0.2 M ZnCl$_2$	—	140	—	0.76	120 cycles (140 h) at 2 mA cm^{-2}	120
Ni$_2$P/CoN–PCP	1.50	0.871	—	—	—	—	—	—	—	—	123
CoO/Co$_x$P	1.6	0.86	0.74	2.0	6 M KOH + 0.2 M Zn(Ac)$_2$	1.4	122.73	—	0.90	400 cycles (200 h) at 5 mA cm^{-2}	124
FeNiP/NCH	1.48	0.75	0.73	1.0	6 M KOH + 0.2 M ZnCl$_2$	1.48	250	—	0.66	2100 cycles (500 h) at 10 mA cm^{-2}	125
Fe$_x$N/NC-7	—	0.885	—	—	6 M KOH + 0.2 M Zn(Ac)$_2$	—	180	668	—	—	129
Co$_4$N@NC-2	1.52	0.84	0.679	1.0	6 M KOH + 0.2 M ZnCl$_2$	1.464	74.3	769.4	0.89	750 h at 5 mA cm^{-2}	130
NC–Co/CoN$_x$	1.52	0.87	0.65	1.2	11.25 M KOH + 0.25 M ZnO (flexible ZAB)	1.40	41.5	—	—	1500 min at 1 mA cm^{-2}	131
Mn$_{0.9}$Fe$_{2.1}$C/NC	1.644	0.78	—	2.0	6 M KOH + 0.2 M Zn(Ac)$_2$	1.5	160	635	—	1000 cycles (334 h) at 5 mA cm^{-2}	134
PB@Met-700	1.56	0.855	0.71	2.0	6 M KOH + 0.2 M Zn(Ac)$_2$	1.41	148	781	—	540 cycles (90 h) at 2 mA cm^{-2}	135
BHPC-950	—	0.81	—	0.5	6 M KOH	1.44	197	797	—	—	142
NHPC$_{1.3}$-900	—	0.87	—	—	6 M KOH + 0.2 M Zn(Ac)$_2$	1.54	207	—	—	—	143
BNPC-1100	—	0.793	—	2.0	6 M KOH + 0.2 M ZnCl$_2$	—	—	—	1.03	600 cycles (100 h) at 2 mA cm^{-2}	144
NPCTC-850	1.73	0.83	0.90	1.0	6 M KOH	1.47	74	730	0.94	180 cycles (30 h) at 5 mA cm^{-2}	145
Co@NCNTA-700	1.51	0.861	0.649	1.0	6 M KOH + 0.2 M Zn(Ac)$_2$	1.484	38.6	368	0.441	1020 cycles (170 h) at 10 mA cm^{-2}	149
Co/Co–N–C	1.54	0.78	0.76	1.0	6 M KOH + 0.1 M Zn(Ac)$_2$	1.41	132	—	1.16	1000 cycles (330 h) at 10 mA cm^{-2}	150
Co@NPCFs	1.63	0.66	0.97	1.0	6 M KOH + 0.1 M Zn(Ac)$_2$	1.44	91.87	611.23	—	80 h at 5 mA cm^{-2}	153
CNF@Zn/CoNC	1.7	0.82	0.88	0.5	6 M KOH + 0.2 M Zn(Ac)$_2$	1.46	140.1	680.2	—	410 cycles (150 h) at 2 mA cm^{-2}	154
CoNC–CNF-1000	1.68	0.80	0.88	—	—	—	—	—	—	—	155
Fe/Co–N/P-9	1.57	0.85	—	1.2	6 M KOH + 0.2 M ZnCl$_2$	1.389	—	565	0.77	130 cycles (21 h) at 5 mA cm^{-2}	156

Table 1 (*Contd.*)

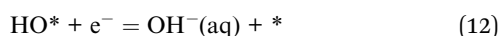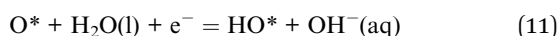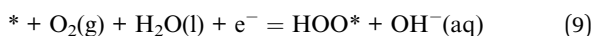| Catalyst	OER performance: E_{10} [V]	ORR performance: $E_{1/2}$ [V]	ΔE [V]	Catalyst loading (mg cm^{-2})	Electrolytes	OCP (V)	Power density (mW cm^{-2})	Specific capacity (mA h g^{-1})	Voltage gap [V]	Cycling performance	Ref.
CoNCNTF/CNFs	1.61	0.857	0.76	—	18 M KOH + 0.2 M Zn(Ac)$_2$ (flexible ZAB)	1.34	63	476.8	0.29	68 cycles (11 h) at 0.5 mA cm^{-2}	157
Co@hNCTs-800	1.63	0.87	0.76	2.0	6 M KOH + 0.2 M Zn(Ac)$_2$	1.45	149	746	0.85	3000 cycles (500 h) at 5 mA cm^{-2}	158
MnO@Co–N/C	1.76	0.83	0.93	—	6 M KOH + 0.2 M Zn(Ac)$_2$	1.43	130.3	—	0.76	1900 cycles (633 h) at 5 mA cm^{-2}	159
CuCoNC-500	1.475	0.84	—	—	6 M KOH + 0.2 M Zn(Ac)$_2$	1.40	140	804	0.80	360 h at 10 mA cm^{-2}	160
GNCNTs-4	1.60	0.85	0.73	1.0	6 M KOH + 0.2 M Zn(Ac)$_2$	1.48	223	—	0.76	2400 cycles (800 h) at 10 mA cm^{-2}	161
FeN$_x$–PNC	1.625	0.86	0.775	—	6 M KOH	1.55	278	—	—	300 cycles (55 h) at 10 mA cm^{-2}	162
CoN$_x$/NGA	1.525	0.83	—	1.0	6 M KOH + 0.2 M Zn(Ac)$_2$	1.33	—	—	—	12 h at 10 mA cm^{-2}	163
Meso-CoNC@GF	1.66	0.87	0.79	1,8	6 M KOH + 0.2 M Zn(Ac)$_2$	1.51	154.4	—	—	630 cycles (105 h) at 20 mA cm^{-2}	164
FeCo-C/N	1.583	0.864	—	2.0	6 M KOH + 0.2 M ZnCl$_2$	1.519	397.25	770.5	0.80	180 cycles (60 h) at 2 mA cm^{-2}	167
NC@Co-NGC DSNCs	1.64	0.82	0.82	0.5	6 M KOH + 0.2 M Zn(Ac)$_2$	1.45	109	565	—	56 h at 10 mA cm^{-2}	168
FeNiCo@NC-P	1.54	0.84	0.70	—	6 M KOH + 0.2 M Zn(Ac)$_2$	1.355	112	807	0.87	120 cycles (120 h) at 10 mA cm^{-2}	169
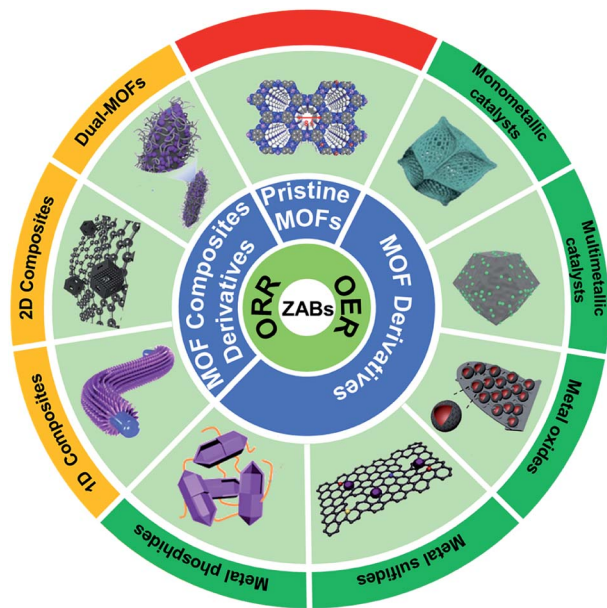
Fig. 1 Scheme organization of the main bifunctional electrocatalysts in this review. Pristine MOFs (HIB-MOF),[59] copyright 2019, Royal Society of Chemistry. MOF derivatives (monometallic catalyst: Fe/OES,[82] copyright 2020, Wiley-VCH; multimetallic catalyst: $Ni_3Fe/Co-N-C$,[94] copyright 2020, Elsevier; metal oxides: $NC-Co_3O_4$,[109] copyright 2017, Wiley-VCH; metal sulfides: Co_9S_8@TDC,[118] copyright 2019, Royal Society of Chemistry; metal phosphide: FeNiP/NCH,[125] copyright 2019, American Chemistry Society). MOF composite derivatives (1D composites: MOF/ENF,[157] copyright 2019, Elsevier; 2D composites: meso-CoNC@GF,[164] copyright 2018, Wiley-VCH; dual-MOFs: FeNi-Co@NC-P,[169] copyright 2020, Wiley-VCH).

usually the first choice for designing advanced ORR electrocatalysts. The reaction mechanisms are shown as follows:

$$* + O_2(g) + H_2O(l) + e^- = HOO* + OH^-(aq) \quad (9)$$

$$HOO* + e^- = O* + OH^-(aq) \quad (10)$$

$$O* + H_2O(l) + e^- = HO* + OH^-(aq) \quad (11)$$

$$HO* + e^- = OH^-(aq) + * \quad (12)$$

The ORR process includes several steps in the air electrode: (1) O_2 diffuses through the pores of the air electrode and is adsorbed on the catalysts; (2) The weakening and breakage of the O–O bond. Among them, the adsorption/desorption
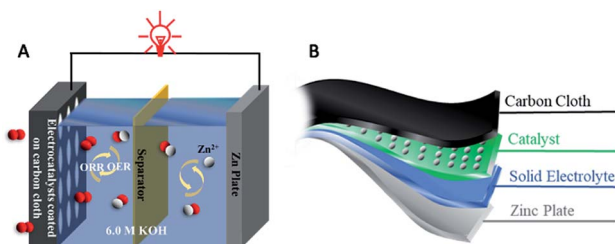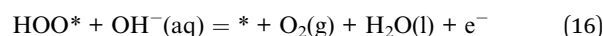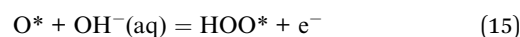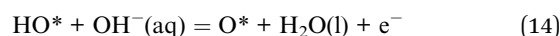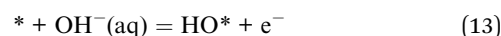

Fig. 2 Schematic diagram of a liquid ZAB (A) and flexible solid ZAB (B).

behaviors of multiple oxygen species such as O*, HOO*, and HO* determine the electrocatalytic performance to a certain extent. According to the Sabatier principle, in a catalytic reaction, the interaction between the catalyst and the reactive species should be neither too strong nor too weak.[44,45] When the adsorption interaction is too strong, the product is difficult to desorb from the surface of the catalysts. When the adsorption interaction is too weak, the reaction species is difficult to combine with the catalysts. Therefore, obtaining appropriate binding energies for the different oxygen intermediates is the key for successful design of an efficient catalyst.

2.3 Reaction mechanisms of the OER

As the reverse reaction of the ORR, the reaction mechanisms of the OER are mainly manifested on the surface of oxides or oxidized metals. Similar to the ORR mechanisms, the OER involves a four-electron transfer process and several oxygen adsorbates are also involved in the reaction, including HO*, O* and HOO*, which are illustrated as follows:

$$* + OH^-(aq) = HO* + e^- \quad (13)$$

$$HO* + OH^-(aq) = O* + H_2O(l) + e^- \quad (14)$$

$$O* + OH^-(aq) = HOO* + e^- \quad (15)$$

$$HOO* + OH^-(aq) = * + O_2(g) + H_2O(l) + e^- \quad (16)$$

The above processes make the overpotential of the OER much larger than the equilibrium potential (1.23 V vs. RHE) and reduce the energy round-trip efficiency greatly. In addition, the over-high potential applied O_2 evolution can induce oxidization of the catalysts and reduce the cycling stability of the catalysts. Therefore, the development of OER catalysts with low overpotentials is essentially important for the performance and lifetime of ZABs.[46–49]

3. MOF-based bifunctional electrocatalysts for Zn–air batteries

As an important class of coordination compounds, MOFs are composed of metal nodes and organic bridging ligands. The periodic structure of MOFs makes the active sites uniformly dispersed throughout the porous framework, and the characteristics of a high surface area and adjustable pore structure make MOFs ideal candidates for bifunctional catalysts (Fig. 3).[50–53] Therefore, the rational design of MOF based catalysts can meet the high standards of ZABs in terms of high catalytic activity and stability. In this section, pristine MOFs, derivatives of MOFs and MOF composites for bifunctional electrocatalysts are reviewed and discussed, respectively.

3.1 Pristine MOFs as electrocatalysts for ZABs

The structural design of MOF-based electrocatalysts follows the principle of a large specific surface area, tunable pore size and rich unsaturated metal centers, to expose more active sites and
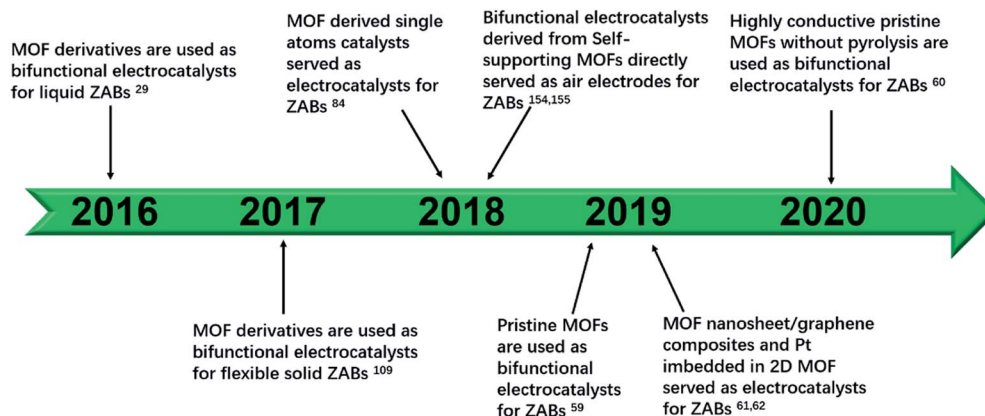
Fig. 3 Time line of important breakthroughs regarding MOF-based electrocatalysis for ZABs.

facilitate mass transport in them.[54–56] In addition, the clear structure and adjustable chemical coordination of MOFs not only bring great convenience to reveal the related catalytic mechanism, but also provide unlimited possibilities for their application in catalysis including using various metal active sites and appropriate ligands to construct conductive MOFs.[11,12,35,57]
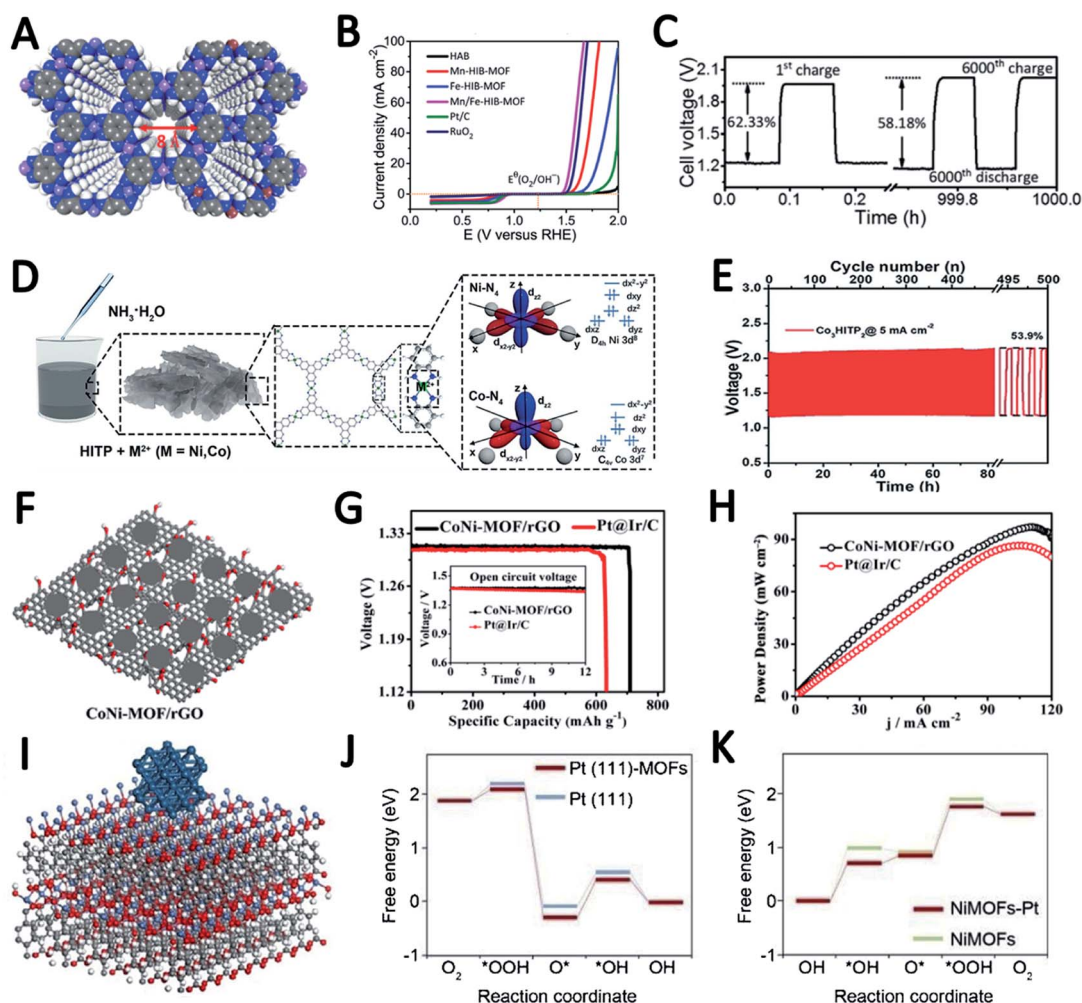

Fig. 4 (A) Structure diagram of Mn/Fe–HIB-MOFs. (B) Bifunctional polarization profiles for the ORR and OER of Mn/Fe–HIB-MOFs. (C) Long-life constant current discharge–charge cycle performance of Mn/Fe–HIB-MOFs. Copyright 2019, Royal Society of Chemistry. (D) Synthesis mechanism of M_3HITP_2. (E) Galvanostatic cycling of Co_3HITP_2. Copyright 2020, Wiley. (F) Structure diagram of CoNi-MOF/rGO. (G) Discharge curve of CoNi-MOF/rGO and Pt@Ir/C based ZABs. (H) Power density curves of the catalysts. Copyright 2019, ACS. (I) Schematic illustrations of Pt@NiNSMOFs. (J and K) Free energy diagrams for ORR and OER pathways in an alkaline medium. Copyright 2019, Elsevier.

In a recent study, 2,3,6,7,10,11-hexaaminotriphenylene reacts with Ni^{2+} in NH_3 aqueous solution to form $Ni_3(HITP)_2$. Dual probe and van der Waals electrical measurements prove that $Ni_3(HITP)_2$ has a good conductivity.[58] Inspired by this work, Lee *et al.* synthesized a new class of 3D dual-linked hexaaminobenzene MOFs (Mn/Fe–HIB-MOFs), which have a unique honeycomb layer structure, as shown in Fig. 4A.[59] Mn/Fe–HIB-MOFs have a huge specific surface area of 2298 m^2 g^{-1}, with high intrinsic electronic conductivity and O_2 adsorption capacity, resulting in the rapid transfer of charge and the fast diffusion of the electrolyte and oxygen. Therefore, Mn/Fe–HIB-MOFs have superior bifunctional performance. The potential gap (ΔE) of Mn/Fe–HIB-MOFs for the ORR and OER is 0.627 V (ΔE means $E_{j=10\ (OER)} - E_{1/2\ (half-wave\ potential\ for\ ORR)}$), which is smaller than the values of commercial Pt/C and RuO_2. The smallest value of ΔE corresponds to its best performance, as shown in Fig. 4B. The authors pointed out that the unique five-shell hollow conjugate system formed by the p orbit of HIB and the d orbit of metal M(II) can improve the intrinsic reaction activity and electron transport, and reduce the overpotentials for the ORR and OER. In addition, the catalyst has a high surface area to enable the rapid transmission of ions and accelerates the oxygen/hydroxyl diffusion, resulting in improved bifunctional performance. Using Mn/Fe–HIB-MOFs as the air cathode for ZABs, the energy density of the battery was measured to be as high as 1027 W h kg_{Zn}^{-1}. Moreover, the long-life galvanostatic charge–discharge cycle performance test demonstrates a very high initial energy round-trip efficiency of 62.33%. Even after 1000 h (6000 cycles), the energy round-trip efficiency is still 58.18% (Fig. 4C), demonstrating its high efficiency and stability.

In another report, Peng *et al.* synthesized a series of bimetallic Ni/Co MOFs by using HITP as a ligand (HITP = 2,3,6,7,10,11-hexaiminotriphenylene) and varying the ratio of metal Ni/Co to investigate the role of metal centers in adjusting the activity of the ORR (Fig. 4D).[60] M_3HITP_2 (M = Co and Ni with various Co/Ni ratios) presents agglomerate particle composed irregular thin nanosheets. Compared with Ni_3HITP_2, the unpaired $3d_z^2$ electrons in Co_3HITP_2 lead to a twisted quadrilateral configuration with less coplanarity, which in turn results in a significant decrease in conductivity. However, the ORR measurements show that Co_3HITP_2 exhibits a higher ORR activity due to the more-active metal centers with unpaired 3d electrons, demonstrating that the 3d orbital configuration of the metal center can promote the ORR. Through calculating the binding energies of intermediates by DFT, it was found that the ORR mechanism undergoes a transition from a two-electron pathway on Ni_3HITP_2 to a four-electron pathway on Co_3HITP_2. In the sequence catalytic performance tests for ZABs, Co_3HITP_2 exhibits a higher output voltage than Pt/C + RuO_2. The specific capacity of the battery catalyzed by Co_3HITP_2 is 784 mA h g_{Zn}^{-1} at 5 mA cm^{-2}, which is 95.8% of the theoretical specific capacity (819 mA h g_{Zn}^{-1}). Galvanostatic cycling tests show that the cycling stability of Co_3HITP_2-based ZABs exceeds 80 h, and the round-trip efficiency eventually remains at 53.9% (Fig. 4E), demonstrating its potential for ZABs. More importantly, M_3HITP_2 is a pyrolysis-free catalyst that directly utilizes

conductive coordination polymers, subverting the perception of poor conductivity of MOFs that are generally not pyrolyzed.

In order to overcome the shortcomings of poor conductivity of pristine MOFs, Zhong *et al.* introduced reduced graphene oxide as a support and prepared bimetallic MOF nanosheets/reduced graphene oxide composites (CoNi-MOF/rGO) (Fig. 4F).[61] This introduction of the rGO structure greatly improves the conductivity of the composites. The pristine MOF nanosheets grown on rGO have a synergistic effect with rGO, and the active sites are exposed to a large extent. These advantages make CoNi-MOF/rGO have a small ΔE of 0.83 V. The high-efficiency catalytic activity of CoNi-MOF/rGO was also reflected by its ZAB performance of a maximum power density (the power density value is based on the peak value of the power density curve, where the power density is the product of voltage and current density) of 97 mW cm^{-2} and a specific capacity of 711 mA h g_{Zn}^{-1} (Fig. 4G and H).

Xia *et al.* developed a bifunctional electrochemical catalyst PtNPs@NSMOFs by embedding platinum nanoparticles into ultra-thin 2D MOF nanosheets containing different transition metals (Fig. 4I).[62] Theoretical calculations based on density functional theory (DFT) reveal that the anchoring of metal–organic groups on the Pt (111) surface can reduce the energy level of the intermediates in the ORR process, thereby improving the ORR catalytic activity of the modified platinum surface (Fig. 4J). In addition, Ni-MOF nanosheets decorated with Pt can weaken the adsorption strength of the OER intermediates on the active site to reduce the energy barrier of the composite catalyst, thereby increasing the OER activity (Fig. 4K). That is, a synergistic effect between Pt NPs and MOF nanosheets through a "win–win" electron structural modification was observed, which can effectively promote the overall OER and ORR performance of PtNPs@NSMOFs. The charge and discharge polarization curves of ZAB using Pt3.2%@NiNSMOFs as an air cathode catalyst show its amazing catalytic performance: the battery has a discharge voltage of 1.450/0.95 V and a charge voltage of 1.606/2.07 V at 10/100 mA cm^{-2}. These values are all better than those of mixed commercial Pt 20%@C (JM) and RuO_2. It is worth mentioning that the ZABs based on Pt3.2%@NiNSMOFs have a maximum power density of 108 mW cm^{-2}, far exceeding that of Pt 20%@C and RuO_2.

Although the above examples show that some pristine MOFs can directly serve as bifunctional catalysts for ZABs, it should be noted that most of the MOFs exhibit poor electrocatalysis performance especially for the ORR due to their poor electrical conductivity, strong internal driving force, and weak chemical stability.[27,63] In addition, the synthesis process for conductive MOFs is relatively complex and the cost is relatively high. Therefore, pristine MOFs for electrocatalysis are still at the exploration stage and more research is needed to develop facile and low-cost preparation routes for conductive MOFs.

3.2 MOF derivatives as electrocatalysts for ZABs

Compared with pristine MOFs, the derivatives of MOFs usually exhibit high conductivity due to the decomposition of the MOFs at high temperatures. The weak coordinate bond in MOFs

makes them also good precursors for designing hollow structured materials.[56,64,65] In addition, the morphology of MOFs can be well inherited, which enables catalysts with well dispersibility and various morphologies. Moreover, MOFs can also act as host materials for external active species by introducing additional metal and non-metal heteroatoms. Therefore, the derivatives of MOFs are more diverse and flourishing.[14,31,34,66]

3.2.1 Monometallic catalysts and single-atom catalysts.

In the preparation of MOF derivatives, the introduction of extra transition metal active centers can offer enhanced electrocatalytic activity of catalysts. Specifically, the metal atoms in the derivatives not only act as active sites themselves, but also can interact with other functional components (such as binding with non-metal atoms) to alter their electronic configuration and improve catalytic performance.[24,31,67,68] Among the bifunctional catalysts based on a single metallic element, the most widely investigated metal is cobalt.[69–71] Because the cobalt atoms can show various oxidation states at ORR and OER potentials and thus exhibit bifunctional activity.[7,72–74]

Xu et al. reported the synthesis of an ultra-long Co-MOF nanotube and transform it into carbon nanofibers wrapped by carbon nanotubes with cobalt nanoparticles on the top (NCo@CNT-NF) by using dicyandiamide as a secondary carbon source and nitrogen source (Fig. 5A).[75] NCo@CNT-NFT exhibits a high specific surface area and large pore volume, and it is rich in pyridine nitrogen, defective graphitized carbon and Co atoms, which can greatly improve the performance of the ORR and OER. Therefore, the catalytic activity of NCo@CNT-NFT is very attractive. The Zn–air battery catalyzed by the optimized catalyst NCo@CNT-NF700 exhibits the best performance with a high open circuit voltage 1.46 V and a maximum power density of 220 mW cm^{-2}. The voltage gap of NCo@CNT-NF700

is 0.8 V, which is much smaller than that of Pt/C (1.05 V) at 50 mA cm^{-2}, as shown in Fig. 5B.

Dai et al. reported Co@N–C named C-MOF-C2 using 3D chiral MOFs (Fig. 5C).[76] C-MOF-C2-900 presents a unique three-dimensional hierarchical rod like structure, with cobalt nanoparticles uniformly distributed on it. X-ray photoelectron spectroscopy (XPS) measurement further indicates the presence of CoO_x and CoN_x species in the carbon network structure. These features greatly enable the high catalytic activity of C-MOF-C2-900. In 0.1 M KOH solution, the ORR half-wave potential ($E_{1/2}$) of C-MOF-C2-900 is 0.82 V, and the OER potential is 1.58 V at 10.0 mA cm^{-2}. The outstanding catalytic performance can catalyze a ZAB with a discharge potential of 1.30 V and a maximum power density of 105 mW cm^{-2} (Fig. 5D).

Typical Co–N–C structural materials have also been extensively investigated using 2D MOFs. Verpoort et al. reported the preparation of Co nanoparticles encapsulated with nitrogen-doped carbon nanotubes (Co–N–CNTs) using a leaf-like 2D bimetallic zeolite imide framework (ZIF-L) as a precursor.[77] By optimizing the Co/Zn mol ratio, Co nanoparticles in the nitrogen-doped carbon nanotubes (Co–N–CNTs) are highly dispersed, and highly active Co–N–C groups are formed. Co–N–CNTs showed a small ΔE value of 0.79 V. When used as bifunctional catalysts for a ZAB, the rechargeable ZAB shows a peak power density of 101 mW cm^{-2} and an initial voltage gap efficiency of 61.1%.

The type of transition metal will affect the catalytic performance of MOF derivatives and even determine whether the catalytic function has diversity. In general, single Cu and Fe metal nanoparticles doped in MOF derivatives can greatly improve the ORR performance of the material. However, this strategy does not contribute much to the catalytic activity of the OER. For example, Chen et al. developed a novel Cu–N/C
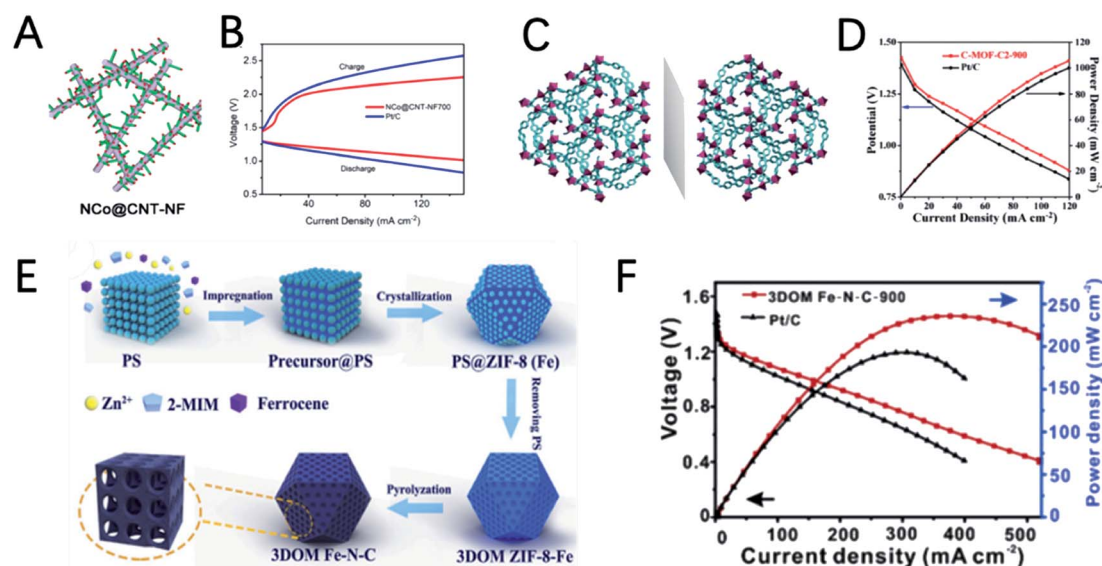

Fig. 5 (A) Schematic diagram of the ORR process of NCo@CNT-NF. (B) Charge and discharge polarization curves of the NCo@CNT-NF and Pt/C based rechargeable ZABs. Copyright 2018, ACS. (C) Enantiomeric packing diagram of the three-dimensional structure of 1L (left) and 1R (right) complexes. (D) Power density curves of C-MOF-C2-900 and Pt/C based ZABs. Copyright 2018, Wiley-VCH. (E) Schematic diagram of 3DOM Fe–N–C. (F) Power density curves of 3DOM Fe–N–C and Pt/C based ZABs. Copyright 2020, Elsevier.

electrocatalyst by directly pyrolyzing Cu-doped ZIF-8.[78] By controlling the loading of Cu, the states of Cu(II) and Cu^0 can be well tuned and $N–Cu(II)–Cu^0$ hybrid coordination sites are successful constructed. Combined with the hierarchical porous structure, high N content and Co–N/C active sites, the ORR performance of 25% Cu–N/C is comparable to that of 30% Pt/C and the ZAB catalyzed by 25% Cu–N/C exhibits a maximal power density of 132 mW cm^{-2}. Unfortunately, the OER activity of the catalyst is not reported.

The Fe element also shows great potential for the ORR in ZABs. Using 3D polystyrene spheres (PSs) as a template to prepare an ordered macro-microporous ZIF-8 precursor and encapsulate ferrocene, Kuang et al. synthesized a 3D hierarchically ordered porous material with highly dispersed FeN_4 active sites (3DOM Fe–N–C), as shown in Fig. 5E.[79] Due to the atomically dispersed FeN_4 and 3D hierarchical structure, 3DOM Fe–N–C-900 exhibits a high half-wave potential of 0.875 V in 0.1 M KOH. In addition, as an ORR catalyst for ZABs, a power density of 235 mW cm^{-2} and a specific capacity of 768.3 mA h g_{Zn}^{-1} were achieved (Fig. 5F).

Recently, single-atom catalysts (SACs) attract great research interest due to their maximum utilization rate of metal atoms and superior catalytic performance. MOFs are good precursors to synthesize SACs due to their periodic crystalline frameworks and atomically dispersed metal nodes, and great progress was

achieved in this area. For example, by using bimetallic ZnCo-ZIFs as precursors and tuning the ratio of Zn/Co, Deng et al. synthesized Co nanoparticles, atomic clusters, and single atoms on an N-doped porous carbon matrix to investigate the size effect of active sites.[80] Among them, the best performance was achieved by single-atom Co catalysts (Co-SAs@NC) (Fig. 6A). The discharge specific capacity of the rechargeable ZAB with Co-SAs@NC is 897.1 mA h g_{Zn}^{-1}, with an open circuit voltage of 1.46 V (Fig. 6B and C). The flexible ZABs catalyzed by Co-SA@NC are applied to power a red-light-emitting diode and a very stable discharge–charge plateaus can be maintained for a long time (Fig. 6D).

Pennycook et al. also developed a cobalt single-atom catalyst (Co-SAC) using 2D Co-MOF nanoflake arrays on carbon cloth as a precursor (Fig. 6E).[81] The uniformly dispersed Co particles and high density of $Co–N_x$ active sites significantly improve the oxygen absorption capacity and mass transfer capacity of the material. The performance of a series of NC–Co SA air electrodes in flat and bent states was investigated by assembling flexible ZABs. As shown in Fig. 6F and G, the peak power density of NC–Co SA in a flat state is 20.9 mW cm^{-2}, and it shows smaller voltage changes during continuous charge and discharge, as well as good cycle stability for up to 600 minutes, indicating that NC–Co SA can tolerate large mechanical changes. NC–Co SA can provide stable power to light-emitting
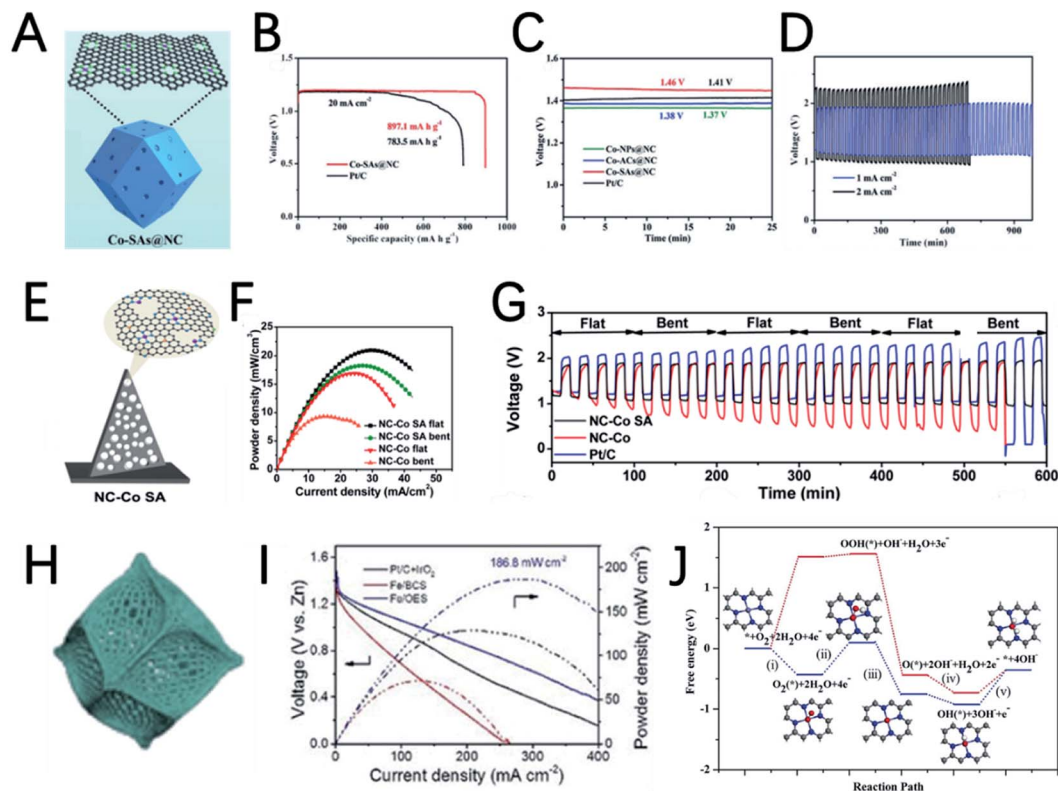

Fig. 6 (A) Schematic diagram of Co-SAs@NC. (B) Discharge curves of Co-SAs@NC and Pt/C based ZABs. (C) Open circuit voltage of the catalysts. (D) Long-term cycling performance of Co-SAs@NC. Copyright 2019, Wiley. (E) Schematic diagram of NC–Co SA. (F) Peak power density curves and (G) charge and discharge polarization curves of NC–Co SA in flat and curved states. Copyright 2018, ACS. (H) Schematic diagram of Fe/OES. (I) Power density curves of Fe/OES based ZABs. (J) ORR free-energy paths of optimized intermediates calculated by DFT (Fe−N₄−C configuration: blue line; V_{FeN_4C} configuration: red line). Copyright 2020, Wiley-VCH.

diodes, regardless of whether in a flat state or a curved state, indicating its extremely promising application prospects.

The morphology of MOFs can usually be well preserved after carbonization. Therefore, the morphology of MOF-derived carbon-based materials can be designed by pre-designing the morphology of MOFs to facilitate the exposure of more active sites. Combined with the highly active single-atom catalytic sites, the performance of the MOF derived electrocatalysts can be further improved. In a recent study, Xu et al. developed a silica-mediated MOF template to prepare an overhang-eave structured (OES) carbon cage decorated with isolated Fe single atoms (Fig. 6H).[82] Thanks to the edge-rich structure with more three-phase boundaries induced by its unique morphology and the combination of iron atoms with adjacent nitrogen/carbon atoms to form Fe–N$_4$–C sites, Fe/OES exhibits superior ORR performance to Pt/C both in 0.1 M KOH and 0.5 M H$_2$SO$_4$. In addition, the ZABs can achieve a capacity of 807.5 mA h g$_{Zn}^{-1}$, and a peak power density of 186.8 mW cm^{-2}, as shown in Fig. 6I. To clarify the origin of the high ORR reactivity, DFT calculations are performed to investigate the free energy for initial oxygen adsorption and the latter four-electron transfer process (Fig. 6J). For Fe–N$_4$–C active sites, the first electron transfer (ii) and the last electron transfer (v) are endothermic, and the highest endothermic energy required is only 0.57 eV(v). In contrast, for iron-free V$_{Fe}$N$_4$C (V$_{Fe}$ stands for Fe vacancies), in

addition to the first (ii) and the last electron transfer steps (v), the oxygen adsorption step (i) is also endothermic and this step requires an endothermic energy of up to 1.52 eV, which is determined to be the rate determining step of the ORR. Therefore, Fe–N$_4$–C is believed to be the real catalytic active site for the ORR and could promote the adsorption of oxygen to facilitate the ORR.

3.2.2 Multimetallic catalysts. Benefiting from the diversity of MOFs' composition, various transition metals can coordinate with organic ligands to form a bimetallic or multi-metallic MOF. Different types/different ratios of metal elements can play a role in inducing electron redistribution,[83,84] preventing sintering and agglomeration of the metal nanoparticles, to achieve the purpose of reducing the reaction overpotential and improving the catalytic activity.[14,31,85–87] In addition, the introduction of multi-metal active centers can overcome the limitation that single metal active sites cannot obtain excellent bifunctional (ORR and OER) activity at the same time.[35,88–91] Furthermore, the synergy between different metals or their interaction with other heteroatoms can further increase the activity of the catalysts.

By proposed pyrolyzing of dopamine coated CoNi-MOF, Deng et al. prepared nitrogen-doped hollow carbon nano-cube coated atomically dispersed Co–Ni active sites (Fig. 7A).[92] Unlike single metal atoms and nanoparticles, the bimetallic-N
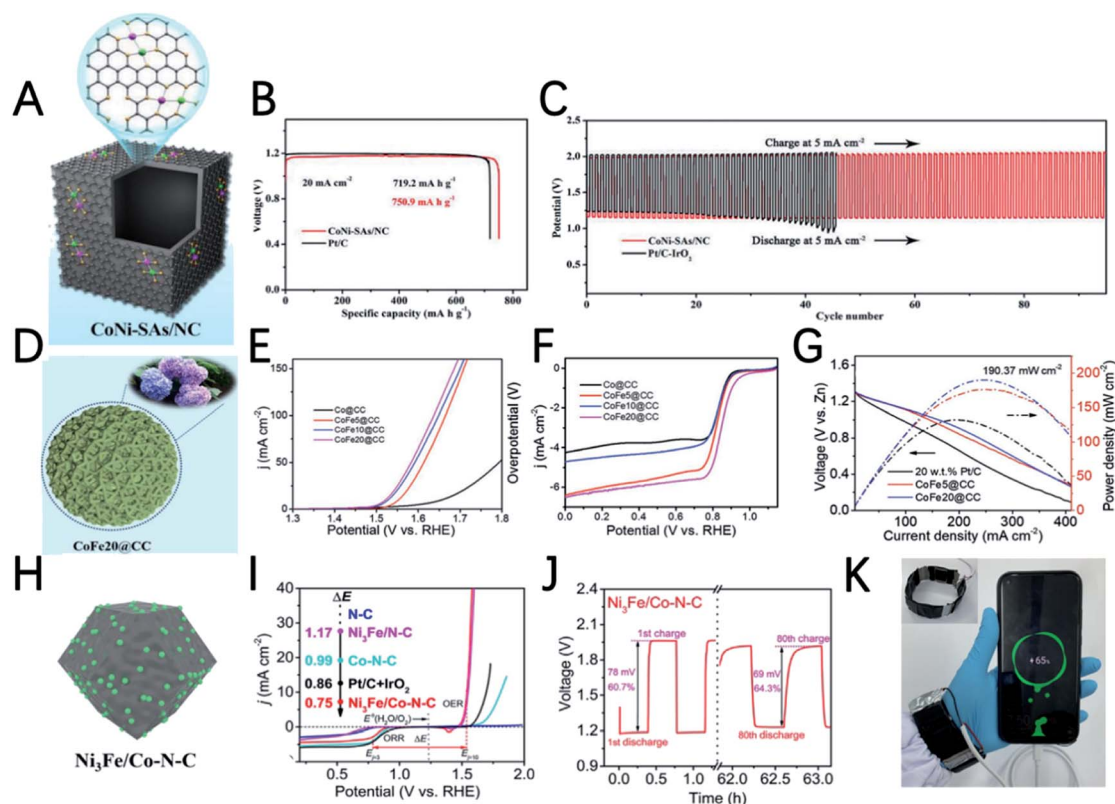

Fig. 7 (A) Schematic illustrations of CoNi-SAs/NC. (B) Discharge curve of CoNi-SAs/NC and Pt/C based ZABs. (C) Discharge−charge performance of a CoNi-SAs/NC based ZAB at 5 mA cm^{-2}. Copyright 2019, Wiley. (D) Schematic illustrations of CoFe20@CC. (E) OER and (F) ORR polarization curves of the CoFe@CC catalysts. (G) Power density curves of the CoFe@CC and Pt/C based ZABs. Copyright 2019, Wiley. (H) Schematic illustrations of Ni$_3$Fe/Co−N−C. (I) The overall polarization curves of the catalysts. (J) The discharge and charge voltage profiles of a Ni$_3$Fe/Co−N−C based ZAB. (K) Four solid-state ZABs are connected in series and used to power mobile phones. Copyright 2020, Elsevier.

structure (Co–Ni–N) of this material can effectively reduce the energy barrier, and the synergy between Co and Ni accelerates the reaction kinetics, resulting in a low overpotential, high electron transfer number and good stability in 0.1 M KOH. The CoNi-SAs/NC based ZAB shows a discharge specific capacity of 750.9 mA h g_{Zn}^{-1}, a low charge and discharge voltage gap of 0.82 V and a high round-trip efficiency of 59.4% (Fig. 7B and C).

By introducing iron ions into the core@shell MOF precursor (ZIF-8@ZIF-67), the derived carbon cages undergo a change in the morphology form the carbon cage to a three-dimensional hydrangea-like structure connected by carbon nanotubes (Fig. 7D).[93] The carbon nanotubes are *in situ* grown on the Fe–Co alloy during the pyrolysis process. Benefiting from the hierarchically porous superstructures induced by the unique morphology and synergetic effects of Co and Fe, CoFe20@CC has an OER overpotential of 291 mV at 10 mA cm^{-2} and an ORR half-wave potential of 0.86 V (Fig. 7E and F). The ZAB equipped with CoFe20@CC has a maximum power density of 190.3 mW cm^{-2} (Fig. 7G), a long lifetime of more than 130 h and a superior cycle stability of 400 cycles.

Taking advantage of the high ORR performance of Co–N–C and high OER activity of Ni$_3$Fe nanoparticles, Tan *et al.* synthesized a trimetallic catalyst by a two-step heat treatment method.[94] Co–N–C was first prepared by thermal annealing of Co-ZIF. Then Co–N–C served as a support to load Ni$_3$Fe nanoparticles (Fig. 7H). Although the ORR half-wave potential of Ni$_3$Fe/Co–N–C shows a 15 mV negative shift compared with that of Co–N–C, the OER overpotential significantly decreased from 580 mV (Co–N–C) to 310 mV (Ni$_3$Fe/Co–N–C). Ni$_3$Fe/Co–N–C also shows the smallest potential gap (ΔE) of the ORR and OER (Fig. 7I). The ZAB based on Ni$_3$Fe/Co–N–C has an initial energy round-trip efficiency of 60.7% and this gradually increased to 64.3% after 80 cycles (>60 h), demonstrating its excellent stability (Fig. 7J). In addition, the flexible ZAB with Ni$_3$Fe/Co–N–C can successfully power a mobile phone, indicating that it has great application potential (Fig. 7K).

The metal–N–C structure has been demonstrated to have good ORR performance. Using appropriate strategies to synthesize metal–N–C electrocatalysts with bimetallic active sites can further enhance the activity of the ORR. Jia *et al.* reported an electrocatalyst FeCo–IA/NC with good ORR activity supported by Fe and Co atoms imbedded in MOF-derived N-doped carbon nanoparticles.[95] FeCo–IA/NC has a large porous surface area and a high content of pyridine N, and the synergistic effect of the isolated FeN$_4$ and CoN$_4$ sites makes it exhibit very good ORR activity (a half wave potential of 0.88 V) and ZAB performance (an open circuit voltage of 1.472 V and a power density of 115.6 mW cm^{-2}). Mu *et al.* prepared Cu@Fe–N–C with rhombohedral dodecahedra by introducing bimetallic ions Fe^{2+} and Cu^{2+} in a MOF followed by pyrolysis at high temperature.[96] The obtained Cu/Fe–N–C structure has uniformly distributed CuFe bimetallic active sites, a large surface area, a high nitrogen doping content and a high conductivity carbon skeleton; therefore it has good ORR performance. The performance of the ZAB with Cu@Fe–N–C achieves an open circuit voltage of 1.48 V and a power density of 92 mW cm^{-2}.
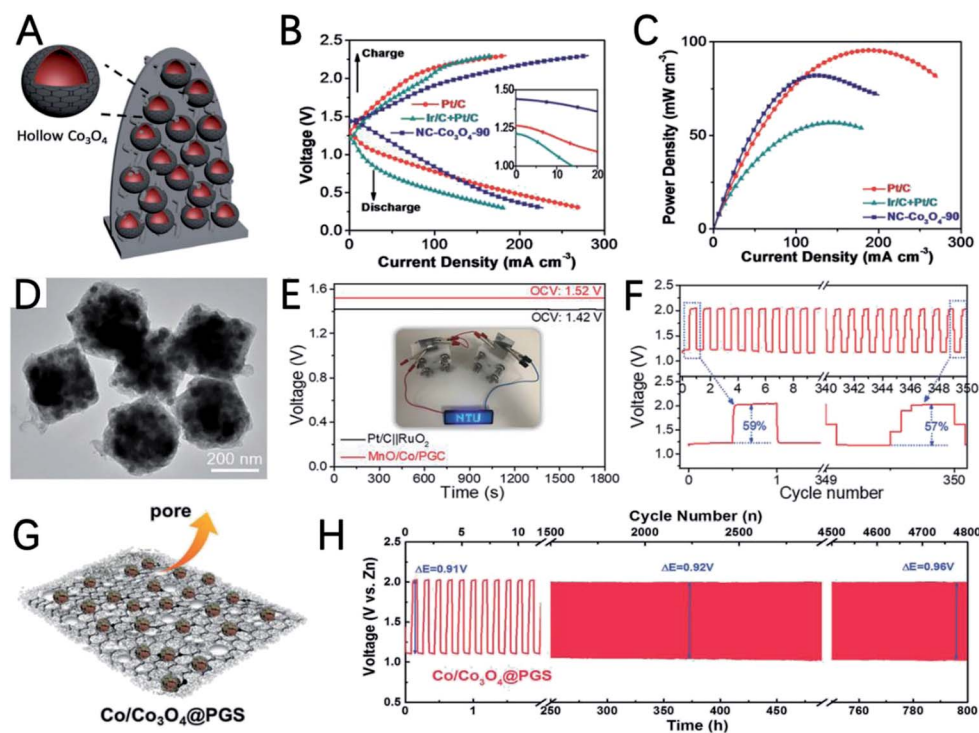

Fig. 8 (A) Schematic illustrations of NC–Co$_3$O$_4$. (B) Discharge and charge polarization curves and (C) power density curve of NC–Co$_3$O$_4$-90 and Ir/C + Pt/C based ZABs. Copyright 2017, Wiley. (D) TEM images of MnO/Co/PGC. (E) Open circuit voltage curves of MnO/Co/PGC and Pt/C∥RuO$_2$ based ZABs. (F) Cycle performance of MnO/Co/PGC based ZABs. Copyright 2019, Wiley. (G) Schematic illustrations of Co/Co$_3$O$_4$@PGS. (H) Long-term cycling performance of Co/Co$_3$O$_4$@PGS based ZABs. Copyright 2018, Wiley.

Promoted by the development of SACs, dual-atom catalysts with higher utilization of atoms and metal loading have emerged. However, till now, there is no investigation about dual-atom catalysts in ZABs, even though some of them have been demonstrated to have very high ORR performance.[97,98] Therefore, the investigation of dual-atom catalysts for ZABs is necessary and it is expected that great progress can be achieved in this area.

3.2.3 Metal oxides. Metal oxides are extremely promising electrocatalysts due to the easy availability, tunable structure and morphology, long-term stability, and high theoretical catalytic activity.[99–101] However, the conductivity of metal oxides limits their catalytic activity.[57,61,102–105] It is worth noting that the use of metal oxides and metal nanoparticle composites, or fixed metal oxides on a highly conductive carbon matrix and other reasonable strategies can effectively promote the internal and surface charge transfer and maximize the utilization of active sites, which can further improve the efficiency of ZABs.[102,106,107]

The weak coordinate bond and uniform morphology of MOFs make them good precursors to prepare hollow nanostructures using the Kirkendall effect.[108] Guan *et al.* improved the synthesis strategy of the Kirkendall effect and synthesized hollow Co_3O_4 nanospheres encapsulated in an N doped carbon nano-wall array ($NC–Co_3O_4$) using carbon cloth supported Co-MOF as a precursor (Fig. 8A).[109] The uneven coverage of the carbon layer on the Co nanoparticles derived by carbonization of the MOF destroys the uniform diffusion of atoms and ions during Co oxidation, and unique irregular hollow Co_3O_4 spheres are obtained. The authors point out that the irregularly shaped hollow Co_3O_4 with a high density of steps and grain boundaries has highly strained and special sites, which can improve the catalytic activity. A solid state ZAB using $NC–Co_3O_4$-90 as the air cathode exhibits a high open circuit potential (1.44 V) and high maximum current density (227 mA cm^{-2}) (Fig. 8B and C), outperforming the performance of Pt/C + Ir/C.

Sometimes, properly constructing a heterogeneous interface can strengthen the interaction between the metal and metal oxide, make full use of the exposed active sites, and promote electron transfer.[102,110] Using bimetallic MOF Co/Mn-MIL-101 as a precursor, Gao *et al.* reported MnO and Co embedded in porous graphite carbon (MnO/Co/PGC) polyhedra for the OER and ORR in ZABs (Fig. 8D).[111] The potential gap between the ORR and OER of MnO/Co/PGC is very small ($\Delta E = 0.82$ V), which reflects its excellent bifunctional oxygen electrocatalytic performance. The ZAB catalyzed by MnO/Co/PGC has an open circuit voltage of 1.52 V and a super-large energy density of 1056 W h kg$_{Zn}^{-1}$ (Fig. 8E). Its energy efficiency only decreased 2% after 350 cycles from 59% to 57% (Fig. 8F), indicating the excellent stability of MnO/Co/PGC. The good performance can be ascribed to: (i) the high ORR activity of MnO; (ii) the *in situ* generated Co nanocrystals have high conductivity and good OER activity and promote the formation of robust graphite carbon; (iii) the strong electron interactions between MnO and Co promote the adsorption/desorption of intermediate products during the oxygen electrolysis process and the homogeneously dispersed MnO/Co heterointerfaces offer extra catalyst–support interaction.

Some mixed materials of metals and metal oxides are heterogeneous catalysts. However, if the interconnectivity between different phases is too weak, it will hinder the process of electron and mass transfer and decrease the bifunctional oxygen electrocatalytic activity and stability.[112] Therefore, it is particularly important to construct an effective atomic scale connection between the phases. Chen *et al.* constructed a mixture of cobalt metal and spinel Co_3O_4 Janus nanoparticles embedded in a porous graphitized shell ($Co/Co_3O_4@PGS$) (Fig. 8G).[113] The interpenetrating multiphase characteristic of this hybrid catalyst can skillfully induce the formation of defective hetero-interfaces. The defect interface captures a large amount of oxygen intermediates, which promotes charge transfer and mass transport. In addition, the N-doped porous 2D carbon network containing Co nanoparticles has the characteristics of high conductivity and a rigid structure. The above characteristics make this material have ultrahigh ORR (half-wave potential of 0.89 V) and OER activity (overpotential of 350 mV) with a ΔE of 0.69 V. The ZAB assembled with $Co/Co_3O_4@PGS$ has a maximum power density of 118.27 mW cm^{-2} and good durability up to 800 h (Fig. 8H).

3.2.4 Metal sulfides. Metal sulfides also have high ORR and OER performance, especially when metal sulfides are imbedded in porous matrices to improve their conductivity.[114–116] In addition, during the preparation process of metal sulfides, the S element can be doped into the carbon matrix, and the catalytic activity of the catalysts can be further improved. Using S- and N-containing organic ligands to construct Co-MOF, Zhang *et al.* prepared a series of Co-MOFs with various morphologies including 1D nanorod, 2D sheet, 3D bulk and 1D nanofiber.[117] After thermal annealing at high temperatures, Co/Co_xS_y imbedded in N,S co-doped carbons are obtained and $Co/Co_x-S_y@SNCF-800$ derived from the 1D nanofiber MOF shows the best performance for the ORR and OER. In another study, Zang *et al.* designed a dual-ligand 2D Co-MOF precursor with N, S and O-containing ligands to prepare N, O, and S-doped tri-doped carbon (TDC).[118] Meanwhile, the Co element in the MOFs is transformed into Co_9S_8 (Fig. 9A). The heteroatom doped carbon shell and highly active Co_9S_8 greatly promote the bifunctional (ORR and OER) catalytic activity of the catalyst. $Co_9S_8@TDC-900$ prepared at 900 °C exhibits a very small OER over-potential of 330 mV at a current density of 10 mA cm^{-2}, and a high ORR half-wave potential of 0.78 V (Fig. 9B and C). The ZAB catalyzed by $Co_9S_8@TDC-900$ has an open circuit voltage of 1.50 V and a maximum power density of 101.5 mW cm^{-2}. Finally, it also has good cycling stability with almost no attenuation for 35 h (Fig. 9D). The utilization of S-containing ligands to construct MOFs is very meaningful and important for it not only simplify the synthetic procedure by the *in situ* vulcanization process, but also could doping S into the carbon to improve the catalytic activity of the carbon substrates.

Ni-based sulfides are also prepared from MOFs and used as catalysts for ZABs. Using nitrogen-doped mesoporous carbon as a template for the growth of Ni-MOF, Fransaer *et al.* reported highly ordered mesoporous nickel sulfides/nitrogen-doped mesoporous carbon (NiS_x/NMC) as a bi-functional catalyst for ZABs (Fig. 9E).[119] The optimized catalyst $NiS_x/NMC-1.5$ has
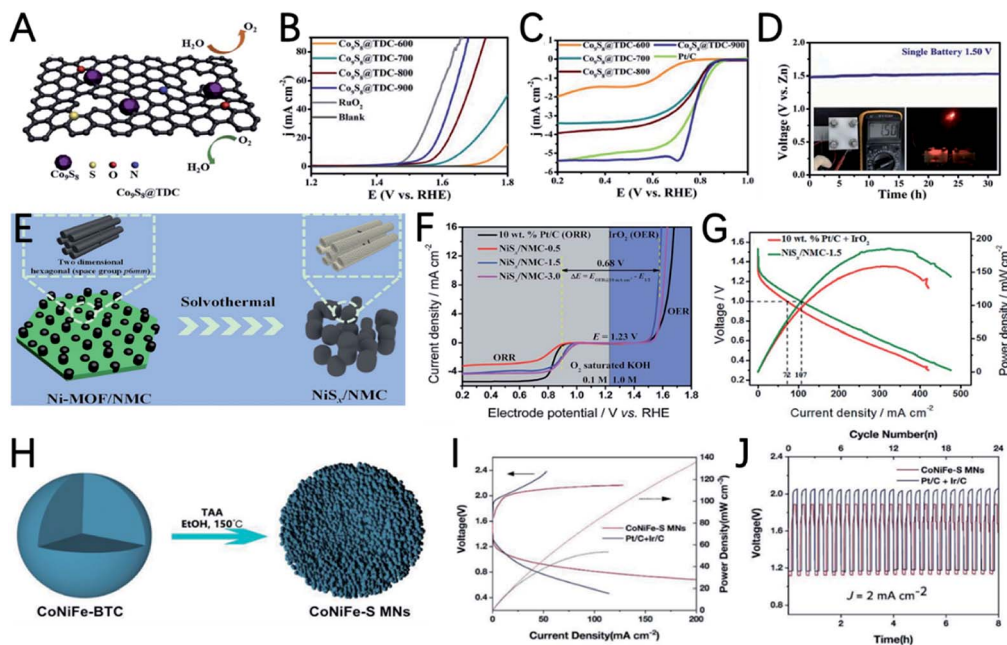
Fig. 9 (A) Schematic illustrations of Co_9S_8@TDC. (B) OER and (C) ORR polarization curves of the Co_9S_8@TDC catalysts. (D) Open-circuit plots of Co_9S_8@TDC-900 based ZABs. Copyright 2019, Royal Society of Chemistry. (E) Schematic illustration of the synthesis of NiS_x/NMC. (F) ORR and OER polarization curves of the NiS_x/NMC catalysts. (G) Power density curves of NiS_x/NMC-1.5 and Pt/C + IrO_2 based ZABs. Copyright 2019, Royal Society of Chemistry. (H) Schematic illustration of the synthesis of CoNiFe-BTC. (I) Galvanodynamic charge and discharge and power density curves and (J) cycling performance of CoNiFe−S MNs and Pt/C + Ir/C based ZABs. Copyright 2018, Wiley.

a high half-wave potential (0.89 V) for the ORR and a low overpotential (340 mV @ 10 mA cm^{-2}) for the OER in 0.1 M KOH solution (Fig. 9F). In addition, the ZAB using NiS_x/NMC-1.5 as an air electrode shows a maximum power density of 186 mW cm^{-2} (Fig. 9G), which exceeds noble metal catalysts.

The variety of metal centers in MOFs also promotes the development of multi-metallic sulfides, and the synergistic effect of different metallic ions can effectively improve the catalytic performance of metal sulfides. The precise control of the ratio of Fe, Co, and Ni to make full use of the synergistic effect of the three metals was demonstrated by Wang's group, where trimetallic CoNiFe-MOF nanospheres were used as precursors to prepare CoNiFe−S mesoporous nanospheres (Fig. 9H).[120] The synergistic effect of trimetallic ions and the high porous structure of the catalyst enables the high OER and ORR performance of CoNiFe−S. The CoNiFe−S involved ZAB exhibits a voltage gap of 0.76 V and a high power density of 140 mW cm^{-3} (Fig. 9I and J).

Although metal sulfides have very high ORR and OER activity, it should be noted that metal sulfides are unstable catalytic active species, especially under strongly OER oxidative conditions.[121,122] For example, XPS spectra of CoNiFe−S after both chronoamperometric and cyclic voltammetry tests indicated the disappearance of metal-S peaks and the positive shift of Co, Ni, and Fe 2p peaks, demonstrating the oxidation of the sulfides to oxides or (oxy)hydroxides.[120] Therefore, it is important to carry out *in situ* analysis to reveal the transfer process and reveal real active sites.

3.2.5 Metal phosphides. Metal phosphides have outstanding OER and HER activity. By anchoring Ni_2P onto a highly active ORR catalyst, Wang *et al.* developed a Ni_2P/CoN–PCP (PCP means porous carbon polyhedron) electrocatalyst.[123] In their work, CoN–PCP was first synthesized by carbonization of ZnCo-MOF. Then the Ni_2P nanoparticles are anchored onto CoN–PCP by thermal decomposition of a mixed precursor consisting of NaH_2PO_2 and $NiCl_2$ in the presence of CoN–PCP. CoN–PCP provides a high ORR activity and large specific area for mass transport. Due to the combination of Co–N and Ni_2P, Ni_2P/CoN–PCP exhibits high activity for the ORR, OER and HER.

Chen *et al.* developed a CoO/Co_xP catalyst through one-step phosphorization of layered cobalt-MOF (Fig. 10A).[124] Interestingly, the heterostructure of CoO/Co_xP significantly improves the electrocatalytic activity through the synergistic effect of cobalt phosphide and cobalt oxide. CoO/Co_xP exhibits a half-wave potential of 0.86 V for the ORR and an overpotential of 0.37 V for the OER, demonstrating its bifunctional activity. The charge–discharge voltage gap of the ZAB with the CoO/Co_xP catalyst (0.90 V) is smaller than that of Pt/C + Ir/C (1.15 V) (Fig. 10B). In addition, the CoO/Co_xP ZAB can provide stable power for the rapid operation of a micro-fan (Fig. 10C).

Xu *et al.* developed an FeNiP/NCH (nitrogen-doped carbon hollow framework) catalyst for ZABs by designing an open-capsular-MOF precursor (Fig. 10D).[125] Due to the unique capsular structure to endow a high electrochemical surface area and electron transfer and highly exposed phosphide sites, FeNiP/NCH shows a good half-wave potential of 0.75 V for the ORR and a very low OER overpotential of 250 mV at 10 mA cm^{-2} (Fig. 10E
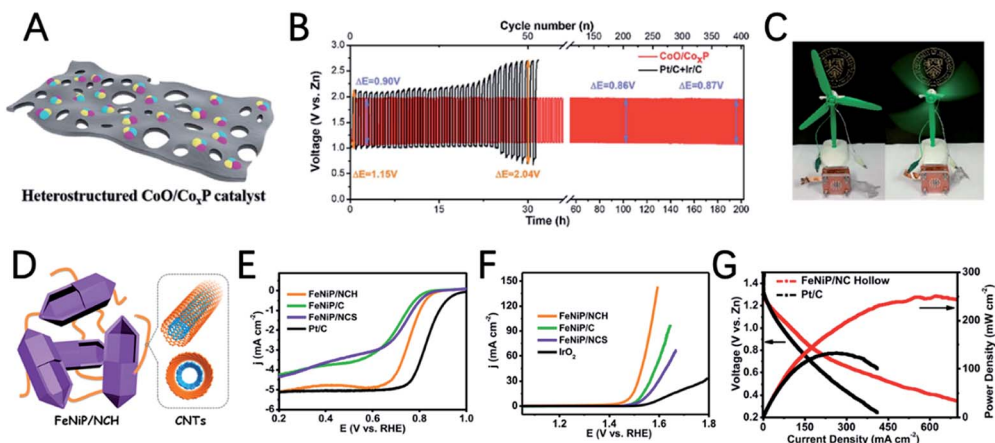
Fig. 10 (A) Schematic illustrations of the CoO/Co$_x$P catalyst. (B) Charge–discharge cycling curves of CoO/Co$_x$P and Pt/C + Ir/C based ZABs. (C) CoO/Co$_x$P based ZABs to power a mini-fan. Copyright 2020, Royal Society of Chemistry. (D) Schematic illustrations of FeNiP/NCH. (E) ORR and (F) OER polarization curves of the catalysts. (G) Power density curves of FeNiP/NCH and Pt/C based ZABs. Copyright 2019, ACS.

and F). The ZAB assembled with FeNiP/NCH shows a maximum power density of 250 mW cm^{-2} (Fig. 10G), charge/discharge voltage gap of 0.66 V and outstanding stability for 500 h.

Although metal phosphides are very promising for the OER, the ORR performance of metal phosphides is poor and metal phosphides need to be combined with other highly active ORR catalysts to achieve bifunctional electrocatalysts for rechargeable ZABs. In addition, the preparation of metal phosphides generally involves the usage of NaH$_2$PO$_2$ as a P source, which is dangerous due to the release of toxic PH$_3$. Therefore, developing

a safe and diversity preparation procedure is desirable and the designing of P-containing ligands may be a suitable strategy.

3.2.6 Metal nitrides. Transition metal nitrides are another class of electrocatalysts with high catalytic performance.[126–128] MOFs can not only meet the requirements of being a precursor for the preparation of metal nitrides, but also can act as a carbon source to prepare an N doped carbon matrix, which can further promote the ORR through the synergistic effect of metal nitrides and the carbon support. Liu *et al.* reported the synthesis of Fe$_x$N embedded in an N-doped carbon material (Fe$_x$N/NC) with excellent ORR activity through pyrolyzing
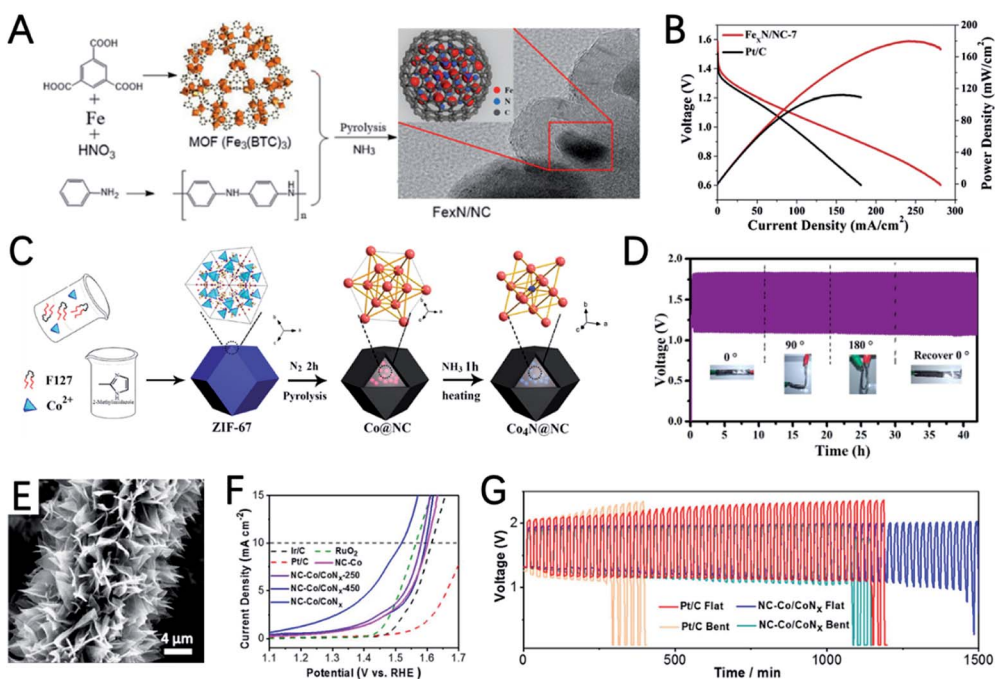

Fig. 11 (A) Schematic illustration of the synthesis of Fe$_x$N/NC. (B) Power density curves of Fe$_x$N/NC and Pt/C based ZABs. Copyright 2020, Elsevier. (C) Schematic illustration of the synthesis of Co$_4$N@NC. (D) Charge–discharge cycling curves of Co$_4$N@NC based ZABs under different bending states. Copyright 2020, Elsevier. (E) SEM image of NC–Co/CoN$_x$ nanoarrays. (F) OER polarization curves of the NC–Co/CoN$_x$ catalysts. (G) Cycling performance of NC-Co/CoN$_x$ and Pt/C based ZABs. Copyright 2019, Elsevier.

$Fe_3(BTC)_3$ under an NH_3 atmosphere (Fig. 11A).[129] $Fe_xN/NC-7$ exhibits a positive half-wave potential of 0.855 V, much higher than that of Pt/C. The synergistic effects of Fe_xN species and the N-doped carbon support and were demonstrated by density functional theory at the molecular level. The primary ZAB assembled using $Fe_xN/NC-7$ displays a peak power density of 180 mW cm^{-2} (Fig. 11B) and a specific capacity of 668 mA h g$_{Zn}^{-1}$.

The high OER activity of metal nitrides was also reported. *Via* two-step pyrolyze of ZIF-67 in N_2 and NH_3, Co_4N nanoparticles encapsulated in nitrogen doped carbon ($Co_4N@NC$) were prepared by Li *et al.* (Fig. 11C).[130] The doping of N into Co nanocrystals can reduce the band gap of Co and enhance the adsorption free energy of Co_4N. The DFT calculation demonstrated the improved electronic conductivity of Co_4N, and greatly decreased the overpotential from *OH to OH$^-$ in the ORR and from *O to *OOH in the OER. As a result, $Co_4N@NC-2$ exhibits outstanding ORR performance with a half-wave potential of 0.84 V and a low OER overpotential of 290 mV. The flexible ZAB assembled with $Co_4N@NC-2$ shows an open-circuit voltage of 1.48 V, a peak power density of 74.3 mW cm^{-2} and stable discharge performance for 83 h at 10 mA cm^{-2} (Fig. 11D).

The heterogeneous interface between cobalt-based nitrides and cobalt atoms/nanoparticles can promote electrocatalysis.[31,128] Wang *et al.* reported the preparation of Co/CoO_x embedded in an N doped carbon nanoarray ($NC-Co/CoN_x$), by carbonization and nitridation of a two-dimensional layered structure Co-ZIF-L precursor grown on carbon cloth (Fig. 11E).[131] $NC-Co/CoN_x$ has a very small OER overpotential of 289 mV at 10 mA cm^{-2} (Fig. 11F), a very high initial potential of 0.93 V and a half-wave potential of 0.87 V for the ORR. The potential gap of $NC-Co/CoN_x$ is only 0.65 V. The outstanding catalytic performance can be ascribed to: (i) the highly active N doped carbon and CoN_x species are very efficient for the ORR and OER; (ii)the interaction between CoN_x and Co enables the high conductivity of the entire electrode; (iii) the various active sites and interfaces provided by the heterogeneous hybrid composed of Co, Co_2N and Co_4N further improve the catalytic performance. The flexible ZAB with the $NC-Co/CoN_x$ cathode can provide very stable potential in both flat and bent shapes (Fig. 11G).

As shown above, there are different coordination numbers of N in metal nitrides and it is difficult to effective control the coordination number to investigated the intrinsic catalytic activity of metal nitrides. In addition, due to the weak crystalline of metal nitrides, it is difficult to determine their crystalline
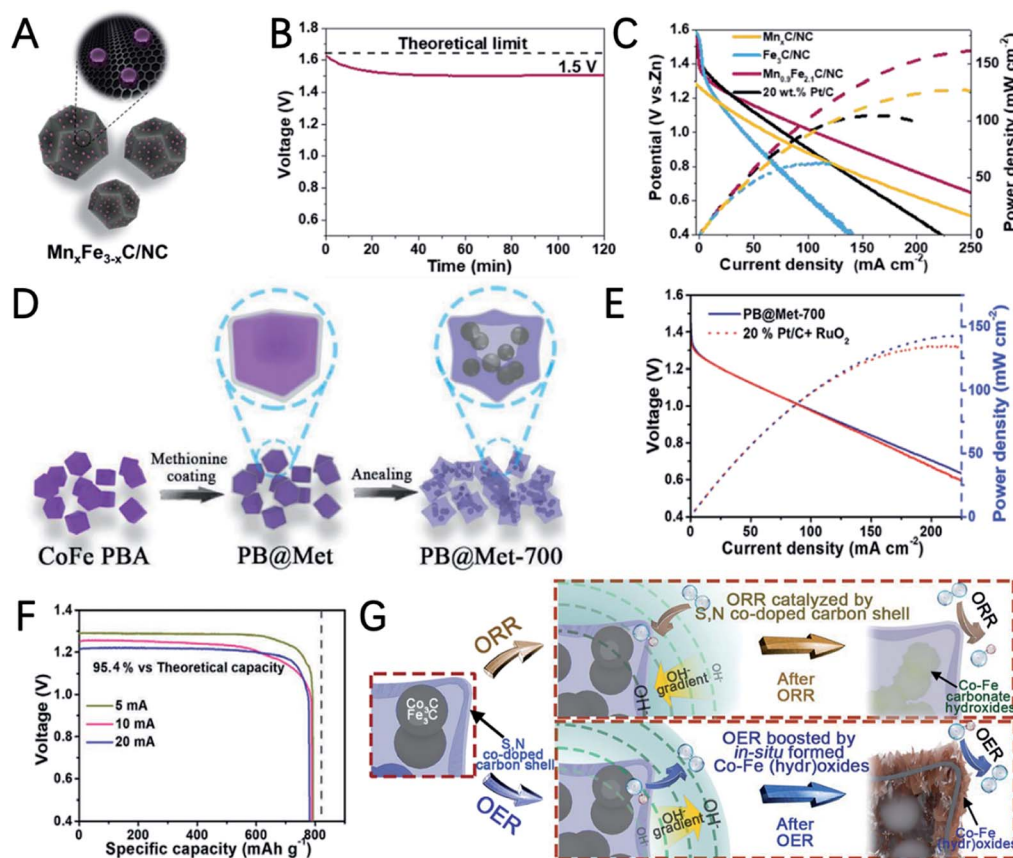

Fig. 12 (A) Schematic illustration of $Mn_xFe_{3-x}C/NC$. (B) Open circuit voltage curve of $Mn_xFe_{3-x}C/NC$ based ZABs. (C) Power density curves of $Mn_xFe_{3-x}C/NC$ and Pt/C based ZABs. Copyright 2019, ACS. (D) Schematic illustration of the synthesis of PB@Met-700. (E) Power density curve of PB@Met-700 and Pt/C based ZABs. (F) Discharge curves of PB@Met-700 based ZABs at different current densities. (G) Schematic diagram showing the source of activity and the evolution of ingredients during the ORR and OER. Copyright 2020, Wiley.

phase and detailed structure. Extended X-ray absorption fine structure (EXAFS) may be a powerful tool to provide clear structure information of metal nitrides and theoretical calculation can be performed to predict their catalytic activity based on different N coordination numbers of metal nitrides.[132]

3.2.7 Metal carbides. Metal carbides especially Fe_3C have been demonstrated as a highly efficient ORR catalyst.[133] To improve the OER performance of Fe_3C, Li et al. incorporated Mn into Fe_3C by using a trimetallic (Fe, Mn, and Zn) ZIF as a precursor (Fig. 12A).[134] The authors point out that the incorporation of Mn can modulate the electronic properties of Fe_3C and the surrounding carbon, and improve the OER activity of $Mn_xFe_{3-x}C/NC$ accordingly. Linear scan voltammetry shows that the doping of Mn can greatly reduce the OER overpotential from 1000 mV for Fe_3C/NC to 414 mV for $Mn_{0.9}Fe_{2.1}C/NC$. A $Mn_{0.9}Fe_{2.1}C/NC$-based ZAB shows a high open-circuit of 1.5 V (Fig. 12B), a maximum power density of 160 mW cm^{-2} (Fig. 12C), and good cycling stability over 1000 cycles.

Peng et al. synthesized S,N co-doped carbon cubic embedding Co_3C/Fe_3C nanoparticles by thermal annealing of a bimetallic cobalt-iron Prussian blue analogue (PBA) coated with methionine (PB@Met) (Fig. 12D).[135] The selection of methionine not only induced S doping, but also avoids the collapse of PBA, and the carbon shows a very high specific surface. XPS measurement indicated the presence of N and S species as well as metal–nitrogen–carbon complexes, which is favourable for improved ORR activity. In addition, the ORR polarization curves of acid washed PB@Met-700 exhibit very similar activity to that of pristine PB@Met-700, suggesting that carbide components are not the main ORR active sites and the S,N co-doped carbon with dispersed M–N–C moieties is responsible for the high ORR activity. The maximum power density of the ZAB assembled with PB@Met-700 is 148 mW cm^{-2} and the specific capacity of PB@Met-700 is 781 mA h g_{Zn}^{-1}, which is 95.4% of the theoretical value (Fig. 12E and F). In addition, the evolution of the catalyst was examined after a prolonged stability test. After an ORR stability test, XRD measurements showed that the diffraction peaks of Co_3C/Fe_3C in the original XRD spectrum disappeared and were replaced with the low-intensity peaks of the Co–Fe carbonate hydroxides due to the oxidation of metal carbides with the participation of O_2 and OH^- at the applied ORR potential. The XRD and TEM analysis of the post-OER catalyst demonstrated the formation of Co–Fe (hydr)oxides, which are believed to be the actual OER active sites. These findings reveal the catalytic mechanisms of metal carbides and can promote the target design and synthesis of metal carbides with high stability for ZABs.

Although the catalytic active sites of metal sulfides, metal phosphides, metal nitrides and metal carbides undergo transformation during the catalytic process, the stability of the catalysts is still decent and this can be explained by the following reasons. Firstly, the metal/metal compounds derived from MOFs are usually encapsulated by carbon, and this could improve the stability of the metal active sites. Secondly, under oxidative conditions, the in situ generated active sites are usually metal (hydro) oxides, and the stability of oxides is good. In addition, it is suggested that strongly coupled carbon and metal oxides could protect the carbon from corrosion to some

extent, though the detailed mechanism is still not clear.[136] In the future, much efforts should be devoted to extensively investigating the stability and durability of bifunctional oxygen electrocatalysts to explore the actual service life of ZABs.

3.2.8 Metal-free carbons. Heteroatom-doped carbon materials are another class of promising electrocatalysts for ZBAs. In traditional synthetic procedures, it is still difficult to accurately control the uniform distribution of doped atoms in the carbon matrix.[137,138] The regular topology and periodical structure of MOFs provide an opportunity for the preparation of porous carbon with very uniform heteroatom distribution.[26,139–141] In addition, the original porous frameworks can be partially reserved after treatment and even evolve into hierarchically porous structures, which is typically different from carbon materials derived from other procedures, where further activation is needed to extend the porosity of the carbons. Moreover, the evaporation of volatile metals could further increase the specific surface area of MOF-based carbons.

As an important kind of MOF, ZIF-8 is composed of Zn^{2+} and 2-methylimidazole. At high temperatures, Zn^{2+} can be reduced to Zn by carbon and evaporated off above its boiling point, which can create many pores on the residual carbon. Therefore, ZIF-8 is a good precursor for the preparation of porous carbons. To further extend the porosity of the ZIF-8 derived carbon, a silica template is used in the crystallization process of ZIF-8.[142] After carbonization and etching of SiO_2, bi-continuous hierarchical porous carbon (BHPC) with macro-meso-microporosity was prepared (Fig. 13A). BHPC exhibits a large specific surface area and unprecedented pore volume and a high N content (7.6 at%), which enable the effective exposure of active sites and continuous mass transfer. The ZAB assembled with BHPC-950 delivers a high capacity of 770 mA h g_{Zn}^{-1} and high-power density of 197 mW cm^{-2} (Fig. 13B and C).

A molten salt-assisted calcination strategy is also used to extend the porosity of carbons derived from MOFs. Wang et al. synthesized three-dimensional nitrogen-doped hierarchical porous carbons (NHPCs) using ZIF -8 precursors as raw materials and NaCl-assisted pyrolysis.[143] NaCl functions as a template and an intercalator and transforms the polyhedral MOF into a three-dimensional nanosheet structure during calcination. Thanks to the intertwined nanosheet structure, abundant micropores and mesopores, high specific surface area and high pyridine nitrogen content, NHPCs exhibit excellent ORR activity for ZABs. The ZAB with $NHPC_{1:3}$-900 has a very high open circuit voltage of 1.54 V and a peak power density of 207 mW cm^{-2}.

Compared with the single element doped system, the multiple heteroatom co-doping strategy can lead to higher OER and ORR catalytic activity due to the synergistic effect of different heteroatoms. By using a MOF containing Zn, N and B as a precursor, Zhao et al. reported B,N co-doped highly porous carbon (BNPC) after thermal annealing under a H_2–Ar mixed atmosphere (Fig. 13D).[144] The introduction of H_2 is important for creating cracked and porous textures. The even distribution of N and B in the carbon matrix could promote the adsorption of hydroxyl ions and water molecules. The optimized catalyst of BNPC-1100 shows a high ORR initial potential of 0.9894 V and
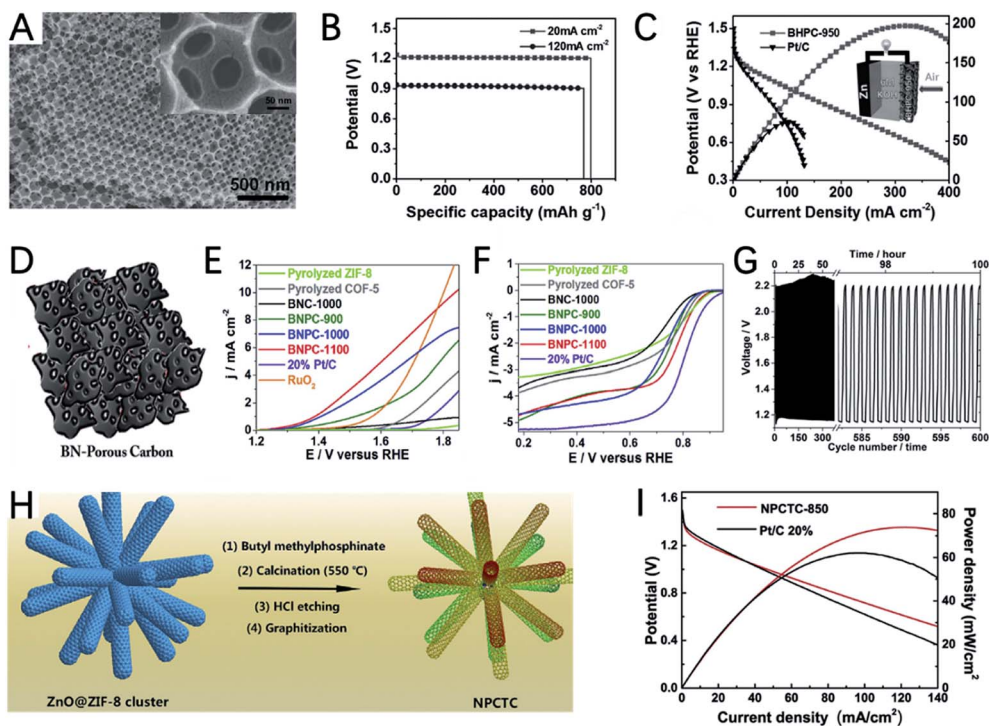
Fig. 13 (A) SEM image of BHPC-950. (B) Discharge curve of BHPC-950 based ZABs. (C) Power density curves of BHPC-950 and Pt/C based ZABs. Copyright 2017, Wiley. (D) Schematic illustrations of BNPCs. (E) OER and (F) ORR polarization curves of the BNPS catalysts. (G) Galvanostatic discharge and charge cycling curves of BNPC based ZABs. Copyright 2017, Elsevier. (H) Schematic illustration of the synthesis of NPCTC. (I) Power density curves of NPCTC-850 and Pt/C based ZABs. Copyright 2018, Elsevier.

a half-wave potential of 0.793 V, as well as a decent OER initial potential of 1.38 V (Fig. 13E and F). As a result, the catalyst demonstrated an acceptable discharge potential of 1.16 V and a charging potential of 2.19 V in a rechargeable ZAB. Although the performance is still not comparable with that of metal-containing catalysts, it also demonstrated the bifunctional activity of metal-free carbons derived from MOFs (Fig. 13G).

Due to the low boiling point of Zn, ZnO is a good template to prepare hollow nanocarbon. In a recent study, Cao _et al._ developed a branched N,P co-doped porous nanotube cluster (NPCTC) by using a ZnO cluster as a template for the growth of ZIF-8 and introducing butyl methylphosphinate for P doping (Fig. 13H).[145] The reduction of ZnO and evaporation of Zn enable the formation of 3D interconnected hollow ultrathin nanotube branches, which can greatly promote electron and mass transfer. The N,P co-doping can create C^+ and P^+ active sites for the adsorption of O_2 and intermediates. Accordingly, NPCTC-850 exhibits a more positive half-wave potential for the ORR than Pt/C, and a lower onset potential for the OER than IrO_2. The open-circuit voltage, peak power density and specific capacity for MPCTC-850 are 1.47 V, 74 mWcm^{-2} and 730 mA h g$_{Zn}^{-1}$ (Fig. 13I), demonstrating its great potential for ZABs.

3.3 Bifunctional electrocatalysts derived from MOF composites

3.3.1 MOFs with 1D substrate composite derived catalysts.
The major disadvantages of MOF-derived catalysts are the

collapse of the skeleton or self-aggregation during high-temperature thermal annealing, which inevitably impede the exposure of active sites and hinder the mass transport.[146] Combining MOFs with 1D nanomaterials could effectively retard the self-aggregation. In addition, 1D substrates made from carbon fibers/nanotubes, metal oxide nanofibers/tubes and polyacrylonitrile have the advantages of a controllable chemical composition, large specific surface area, high porosity, and excellent mechanical strength, which can improve mass transport in the catalysts and stability of the catalysts.[147,148] Moreover, by designing MOF composites, the amount of MOF in the precursors could be reduced, which is beneficial for decreasing the cost of the electrocatalysts due to the high cost of MOFs.

Carbon cloth (CC) has good flexibility and high conductivity and can be used as a flexible and highly conductive substrate for the growth of bifunctional electrocatalysts. By _in situ_ growth of ZIF-67 on CC, cobalt nanoparticles embedded in an N doped carbon nanotube array (Co@NCNTA) were developed by Zhu _et al._ for flexible ZABs (Fig. 14A).[149] As a self-supporting electrode for ZABs, the reduction of catalytic activity induced by the utilization of polymer binders was avoided. The three-dimensional interconnected porous structure with high conductivity can promote charge transfer and mass transfer in the catalytic process. In addition, a large number of N dopants and atomically dispersed Co sites in the catalyst promote the catalytic activity of Co@NCNTAs. The catalytic performance of Co@NCNTA-700 in ZABs surpasses that of noble catalysts of Pt/
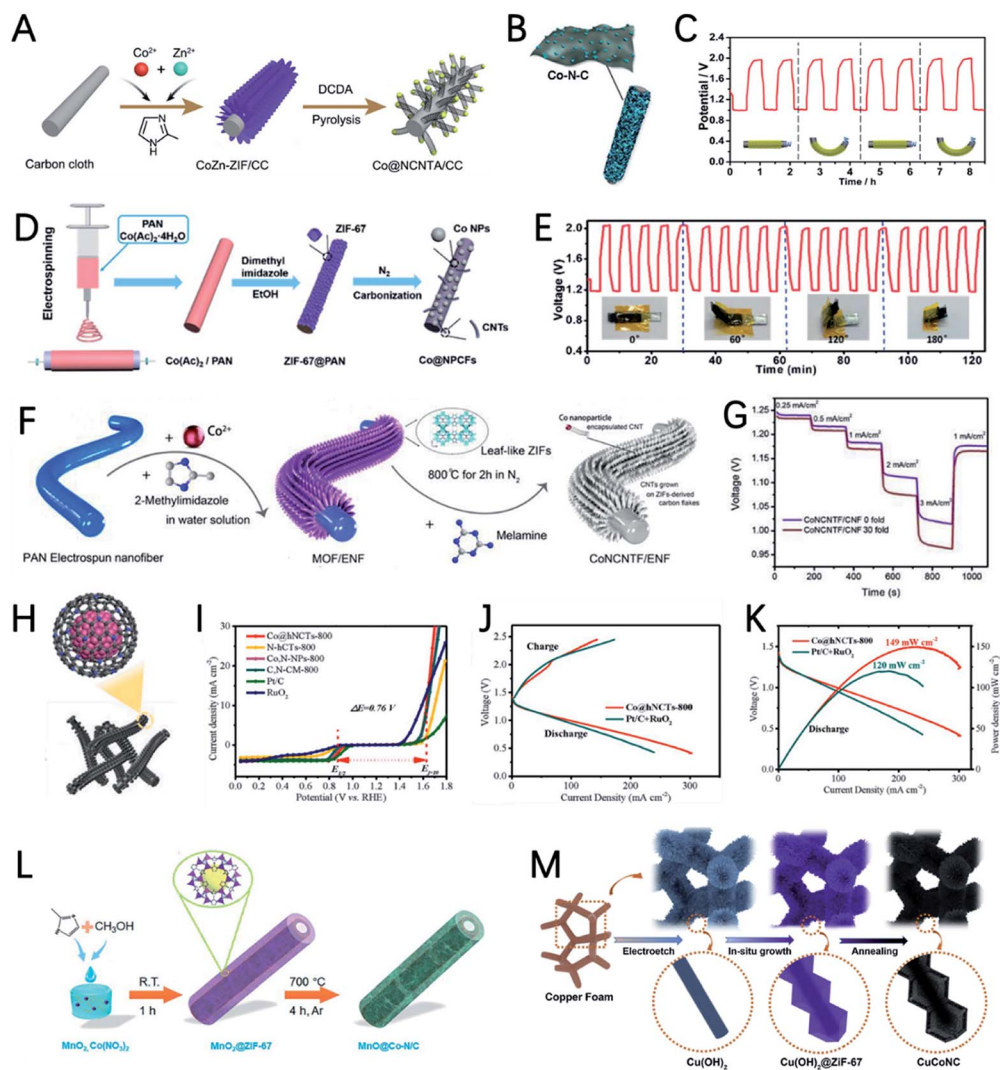
This journal is © The Royal Society of Chemistry 2020

Chem. Sci., 2020, **11**, 11646–11671 | **11663**

Fig. 14 (A) Schematic illustration of the synthesis of Co@NCNTA/CC. Copyright 2020, Wiley. (B) Schematic illustrations of Co/Co−N−C. (C) Charge and discharge cycle curves of Co/Co−N−C based ZABs under different bending states. Copyright 2019, Wiley. (D) Schematic illustrations of the synthesis of Co@NPCFs. (E) Galvanostatic cycling performance of the solid-state ZABs with Co@NPCFs. Copyright 2020, Royal Society of Chemistry. (F) Schematic illustration of CoNCNTF/CNF. (G) Discharge curves of CoNCNTF/CNF based ZABs at different current densities. Copyright 2019, Elsevier. (H) Schematic illustration of Co@hNCTs. (I) ORR and OER polarization curves of the Co@hNCT catalysts. (J) Charge and discharge polarization curves of Co@hNCTs-800 and Pt/C + RuO$_2$ based ZABs. (K) Discharge polarization and power density curves of Co@hNCTs-800 and Pt/C + RuO$_2$ ZABs. Copyright 2017, Elsevier. (L) Schematic illustration of the synthesis of MnO@Co−N/C. Copyright 2018, Royal Society of Chemistry. (M) Schematic illustration of the synthesis of CuCoNC. Copyright 2020, Elsevier.

C + Ir/C, and it can work at external stress without obvious loss of the electrochemical performance. Similarly, by electrodeposition of Co nanosheets on carbon felt and *in situ* growth of ZIF-67, Wang *et al.* synthesized Co nano-islands on Co−N−C nanosheets (Co/Co−N−C) supported by carbon felt (Fig. 14B).[150] The Co nano-islands contact well with Co−N−C nanosheets in Co-/Co−N−C, where the presence of Co and Co^{2+} dual active centers facilitates the improvement of ORR and OER performance. The self-supporting catalyst can be directly used as a ZAB electrode without an additional binder, thus greatly enhancing the electrical conductivity and performance of the air electrode. The peak power density of the Co/Co−N−C catalyst is 132 mW cm^{-2}, which is better than that of Pt/C under the same conditions. It is worth mentioning that, at a current density of 5 mA cm^{-2}, the

prepared battery was repeatedly bent and flattened for 9 h, and there was no obvious performance loss (Fig. 14C).

As a low cost and readily available polymer, polyacrylonitrile (PAN) nanofibers are also a common support for the growth of MOFs. In addition, the highly conductive porous carbon fiber obtained after pyrolysis of PAN can facilitate the electron transfer during electrocatalysis processes.[147,151,152] Traditional, the PAN nanofiber can be readily prepared *via* an electrospinning technique, and during this process, metal ions can be introduced into the PAN nanofiber. Then PAN@MOF composites can be obtained after immersing the PAN nanofiber into ligand solutions. Using this strategy, Huo *et al.* first prepared Co(Ac)$_2$/PAN nanofibers (Fig. 14D).[153] Then these fibers were immersed in EtOH solution containing 2-methylimidazole for

the coordination of Co^{2+} to form PAN@ZIF-67. After carbonization, binder-free and self-standing electrodes composed of Co nanoparticles imbedded in N doped carbon nanofibers (Co@NPCFs) are prepared. The Co nanoparticles provide rich active sites for the ORR and OER and the graphitic carbon nanofiber can promote electron transfer, oxygen capture and desorption of OH^-. The flexible ZABs can deliver an open-circuit voltage of 1.33 V and provide stable voltage for more than 120 h at different bending angles (Fig. 14E). In Liang's work, the nucleation and growth process of ZIF-67 on PAN nanofibers was systematically investigated and the size of ZIF-67 can be well controlled, which can provide more precise methods of controllable synthesis of PAN@ZIF-67.[154] In another report, 2-methylimidazole (MeIM) in PAN nanofibers (PAN-MeIM) was first prepared and Zn, Co-ZIF is grown on the nanofiber to further extend the porosity of the catalysts.[155] Similarly, Ma et al. prepared ZIF-67@PAN nanofibers and adding extra $FeCl_3$ and hexachlorophosphazene (HCCP) in the electrospinning process to provide extra Fe, N and P active sites.[156] The obtained catalyst Fe/Co–N/P-9 also shows high catalytic performance for ZABs.

In contrast, Li et al. first prepared a PAN nanofiber film without metal ions and ligands.[157] After immersing the PAN nanofiber film into the mixtures of $Co(NO_3)_2$ and 2-methylimidazole, leaf-like ZIF-67 is grown on the PAN (Fig. 14F). After the carbonization process assisted by melamine, cobalt decorated carbon nanotubes/porous carbon flake arrays (CoNCNTF/CNFs) were prepared. The unique hierarchical microstructure provides a large number of active sites for the OER and ORR as well as fast mass and charge transfer. Expectedly, the potential difference between the ORR and OER is only 0.76 V and the assembled flexible ZAB exhibits a high capacity of 476.8 mA h g_{zn}^{-1} and a peak power density of 63 mW cm^{-3}. Discharge curves at different current densities and different degrees of bending also show that it has good stability and good bending performance (Fig. 14G).

Using polypyrrole (PPy) nanotubes as a structure-guiding template for the in situ growth of ZIF-67 followed by high temperature carbonization, Co nanoparticles encapsulated in hollow nitrogen-doped carbon tubes (Co@hCNTs) were synthesized by Zhao et al. TEM results show that the Co nanoparticles are evenly dispersed on the carbon nanotube to form a corn-like Co–N–C catalyst (Fig. 14H).[158] The highly conductive carbon framework with hierarchical microporous and mesoporous structures not only guarantees a high surface-to-volume ratio, but also provides fast electron and ion transfer. Co@hCNTs-800 has a small potential gap of 0.76 V (Fig. 14I). The charge–discharge curve shows that the charging performance of Co@hNCTs-800 is equivalent to that of Pt/C + RuO_2, while the discharge performance is better than that of Pt/C + RuO_2 (Fig. 14J). In addition, the maximum power density of Co@hNCTs-800 is 149 mW cm^{-2} (Fig. 14K), which is higher than the 120 mW cm^{-2} of Pt/C + RuO_2.

MOF and metal oxide (hydroxide) composites are also good candidates for the preparation of bifunctional catalysts and metal oxides (hydroxides) can introduce extra active sites. Using ultra-thin MnO_2 hollow nanowire supported ZIF-67 as a precursor, Xie et al. prepared Co–N/C on MnO nanowires as

a catalyst for ZABs (Fig. 14L).[159] The MnO coated with a highly conductive carbon layer greatly inspired its catalytic activity due to the improved electron transfer. The hollow 1D MnO_2 nanowire template can effectively reduce the aggregation of the Co–N/C carbon skeleton and promotes electron and mass transfer. As a result, solid-state Zn–air batteries catalyzed by MoO@Co–N/C can deliver a high open circuit voltage of 1.43 V with high rate performance and stability. Peng et al. assembled Co-MOF (ZIF-67) nanoparticles on $Cu(OH)_2$ nanowires and prepared a CuCoNC nanowire array on Cu foam (Fig. 14M).[160] The catalyst contains multiple active sites such as Co and Cu nanoparticles, CoO_x and the Co–N–C complex, which greatly contribute to its catalytic activity. The overpotential for the OER at 10 mA cm^{-2} is as low as 245 mV and the ORR performance is comparable to that of Pt/C. The ZAB assembled with CuCoNC-500 exhibits a maximum power density of 140 mW cm^{-2}, charge and discharge voltage gap of 0.8 V and round-trip efficiency of 59%.

3.3.2 MOFs with 2D substrate composite derived catalysts.
Graphene is the most commonly used 2D substrate for the growth of MOFs, due to the abundant O-containing motifs for the adsorption of metal ions. In addition, graphene with high electrical conductivity and a 2D nanosheet structure can further facilitate the electron transfer and exposure of active sites. A graphene oxide (GO) layer is used as a 2D substrate for the in situ growth of ZIF-67 by Xia et al. And by further annealing of the ZIF-67@GO composite in a reductive atmosphere, a 2D graphene/N doped carbon nanotube hybrid (GNCNT) was prepared and used a catalyst for ZABs (Fig. 15A).[161] The 2D hierarchical structure with rich Co–N–C active species boost the ORR and OER performance of the GNCNTs. High power densities of 253 mW cm^{-2} and 223 mW cm^{-2} were achieved in liquid and flexible solid state ZABs, respectively. ZABs equipped with GNCNTs-4 has a very high specific capacity of 801 mA h g_{zn}^{-1} at 5 mA cm^{-2} and 728 mA h g_{zn}^{-1} at 10 mA cm^{-2}, respectively (Fig. 15B). Using polypyrrole as a binder for the uniform growth of ZIF-8 on graphene and coordinating iron ions with 2,2-Bipy on the surface of ZIF-8, Zhi et al. prepared a single-site Fe–N_x active species on highly graphitized two-dimensional N doped porous carbon (FeN$_x$–PNC) as a catalyst for ZABs (Fig. 15C).[162] The single-site dispersed Fe–N_x species and abundant N-containing motifs serve as highly efficient active sites, and the graphene acts as a highly conductive carbon substrate for charge transfer. Therefore, the potential gap between the ORR and OER of FeN$_x$–PNC is only 0.775 V, indicating its superior bifunctional catalytic activity. Moreover, a compressible and bendable ZAB assembled with the FeN$_x$–PNC cathode exhibits a charge–discharge voltage gap of 0.78 V and can worked under mechanical deformations of compressibility and bending with no degradation in performance (Fig. 15D). A hierarchical porous graphene aerogel (GA) was also used as a host for the in situ growth of ZIF-67, and the formed CoN_x and N_xC sites after annealing greatly improve the catalytic performance of GA, further demonstrating the advantages of MOF/graphene composites.[163]

Using in situ characterization to reveal the electrocatalyst active sites and mechanisms for ZABs is very significant. Yan et al. prepared a heteroatom doped porous carbon by using
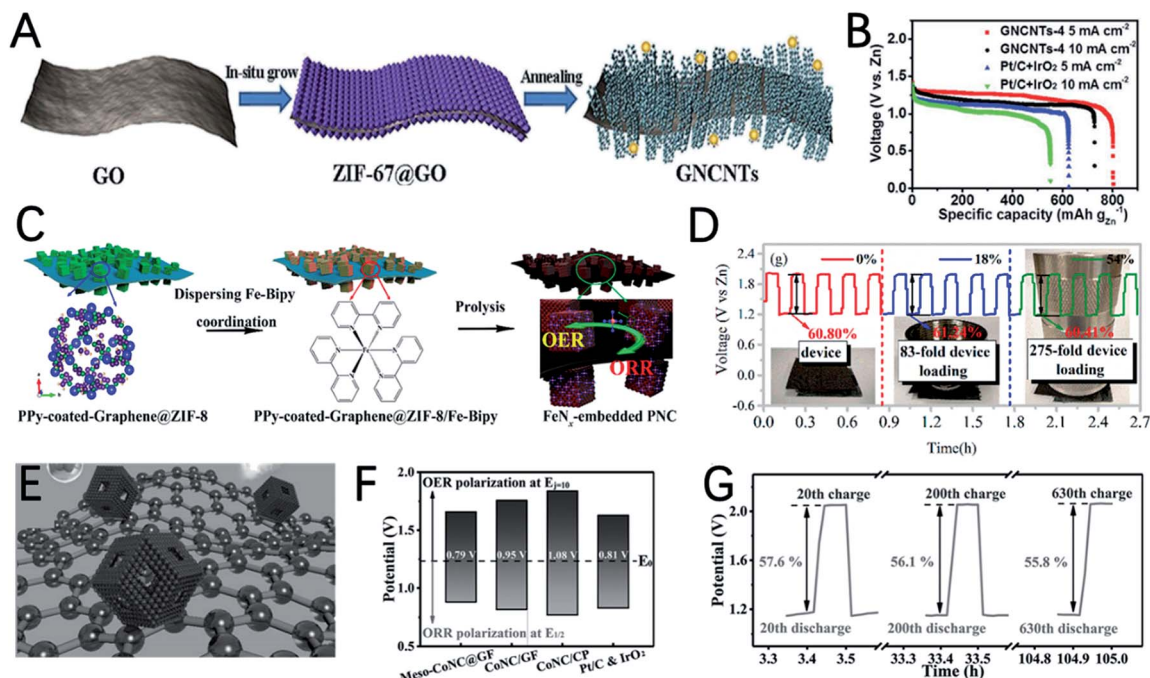
Fig. 15 (A) Schematic illustration of the synthesis of GNCNTs. (B) Discharge curves of GNCNTs-4 and Pt/C + IrO_2 based ZABs at 5 and 10 mA cm^{-2}. Copyright 2020, Wiley. (C) Schematic illustration of the synthesis of FeN_x–PNC. (D) Galvanostatic discharge–charge cycling curves of FeN_x–PNC based ZABs at different compression strains. Copyright 2018, ACS. (E) Schematic illustrations of *meso*-CoNC@GF. (F) The potential gap ΔE of the catalysts. (G) Cycle performance of the *meso*-CoNC@GF based ZAB. Copyright 2018, Wiley.

a Co, Zn, and N-containing ligand MOF/graphene framework composite as a precursor (Fig. 15E).[164] The *in situ* observations indicate that doping N atoms can cause electron deficiencies in the carbon-based catalyst and facilitate chemisorption of O_2 and O-containing intermediates on the porous carbon, and thus the oxygen reaction activity for ZABs is improved. The outstanding ORR and OER performance of *meso*-CoNC@GF is reflected by its small ΔE value (0.79 V) (Fig. 15F). The ZAB equipped with *meso*-CoNC@GF shows extremely strong cycle stability. The energy round-trip efficiency only lost 1.8% from 57.6% in the 20th cycle to 55.8% in the 630th cycle (Fig. 15G). This work provides a deep understanding of the reaction mechanism for heteroatom doped carbon in ZABs, and points out the direction for further research.

3.3.3 Dual-MOF derived catalysts. The catalytic activity of MOF derivatives can be further improved by designing dual or multi-MOF composites to enhance their intrinsic activity from the synergetic effect of multiple metal components.[77,165,166] ZIF-L is a 2D leaf-shaped MOF, which has a large surface area and abundant uncoordinated metal–ligand sites. Taking advantage of the leaf-like ZIF-L as a core, by further growing a ZIF-8 shell on the outside and encapsulating 5,10,15,20-tetraphenylporphyrinatoiron (FeTPP) as an Fe source, Cao *et al.* synthesized an FeCo bimetallic material embedded in nitrogen-doped porous carbon (FeCo–C/N) for the ORR (Fig. 16A).[167] DFT calculations indicate that iron in FeCo–C/N can boost ORR activity by reducing the formation energy of *OOH. The ZABs equipped with FeCo–C/N have a peak power density of 397.25 mW cm^{-2} and excellent charge and discharge performance (Fig. 16B). This report provides

a new way for the synthesis of two-dimensional MOFs with a yolk–shell structure to be used as a cathode catalyst for ZABs.

3D structured ZIF-8 and ZIF-67 can also be used to prepare core–shell structured dual-MOF nanocomposites. Qiu *et al.* using ZIF-8 polyhedrons as a core for the epitaxial growth of ZIF-67, core–shell ZIF-8@ZIF-67 polyhedrons are prepared and used as precursors for the preparation of a core–shell N doped carbon @ Co–N doped graphitic carbon (NC@Co–NGC) catalyst (Fig. 16C).[168] The inner NC core formed by the carbonization of ZIF-8 benefits the diffusion kinetics and the outer shell Co–NGC derived from ZIF-67 provides high catalytic activities. DFT calculations show that the high density of uncoordinated hollow-site C atoms with respect to the Co lattice in Co–NGC can effectively adsorb the OOH* intermediate and induce good bifunctional electrocatalytic activity. Therefore, Co–NGC DSNCs exhibited excellent OER and ORR catalytic activities with a low OER overpotential of 420 mV at 10 mA cm^{-2} and a high ORR half-wave potential of 0.82 V (Fig. 16D and E).

Chen *et al.* reported the synthesis of Fe_2Ni_MIL-88@ZnCo_ZIF composites as precursors for the preparation of Fe–Ni–Co metal/metal phosphide nanoparticles embedded in N doped carbon nanorods (FeNiCo@NC–P) (Fig. 16F).[169] This hybrid material has many advantages: (i) the synergistic effect of multimetal/metal phosphide nanoparticles promotes charge transfer and mass transport; (ii) nitrogen-doped carbon has high conductivity and a certain ORR activity; (iii) the micro/mesoporous structure fully relieves the concentration polarization during the catalytic oxygen reaction process while ensuring sufficient active sites and effective oxygen and electrolyte
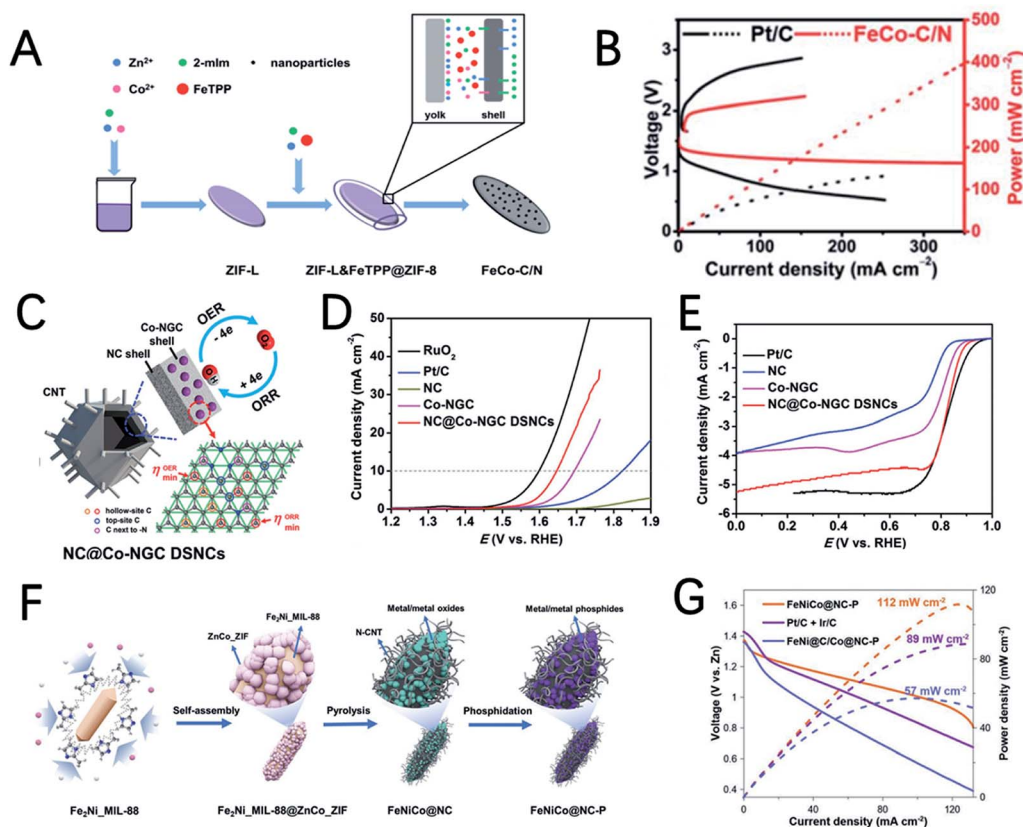
Fig. 16 (A) Schematic illustration of the synthesis of FeCo−C/N. (B) Polarization curves of FeCo−C/N and Pt/C based ZABs. Copyright 2020, Royal Society of Chemistry. (C) Schematic illustration of NC@Co-NGC DSNCs. (D) OER and (E) ORR polarization curves of the catalysts. Copyright 2017, Wiley. (F) Schematic illustration of the synthesis of FeNiCo@NC-P. (G) Power density curves of FeNiCo@NC-P, mixtures of FeNi@C and Co@NC-P, and Pt/C + Ir/C based ZABs. Copyright 2020, Wiley.

diffusion; (vi) the heterogeneous interface reduces the interfacial resistance and further promotes charge transfer. As a result, the ZAB equipped with FeNiCo@NC-P has a specific capacity of 807 mA h g_{Zn}^{-1} and a peak power density of 112 mW cm^{-2}, which are significantly higher than those of Pt/C + Ir/C (Fig. 16G).

4. Conclusions and outlooks

In conclusion, MOF based bifunctional electrocatalysts have demonstrated great potential for ZABs due to their tailored metal centers and organic ligands, regular structures with periodic crystalline frameworks of MOFs. Rational regulation of the compositions and structures of MOFs can provide electrocatalysts with high performance in terms of activity and stability. Indeed, MOF based electrocatalysts are the focus of current research and a class of the most promising candidates for practical applications.

As can be seen from the above cases, the electrocatalysts derived from MOFs usually possess a very high specific surface and can inherit the morphologies of the MOF precursors, which can provide abundant active surface sites and fast mass transport for the ORR and OER. In addition, by designing different synthetic procedures, various active species such as metals or

their alloys, metal oxides, metal sulfides, metal phosphides, metal nitrides, and metal carbides can be obtained. And the various active species usually show different catalytic activity for different reactions. Therefore, we can design multiple active species in an electrocatalyst to boost both the OER and ORR performance of the catalyst. Moreover, by combining MOFs with an extra template such as SiO$_2$, electrocatalysts with a hierarchical structure and improved specific surface area can be obtained, and the catalytic performance of the electrocatalysts can be expected to be further improved. Last but not least, combining MOFs with 1D or 2D substrates could effectively avoid the aggregation of MOF derived electrocatalysts upon thermal annealing, and the substrates could also provide extra active sites and improve the conductivity of the catalysts.

Although great progress has been achieved in MOFs and their derivatives for ZABs, it should be pointed out that there are still great challenges for practical applications of MOF based electrocatalysts in both scientific and industrial fields.

Firstly, as discussed above, the most investigated electrocatalysts are the derivatives of MOFs rather than MOFs themselves. The real charming characteristics of MOFs are their various topologies, regular periodic skeletons, and crystalline porous frameworks. However, these unique advantages of MOFs are more or less destroyed upon thermal annealing.

Therefore, the direct utilization of pristine MOFs as pyrolysis-free catalysts is attractive. The main limitations of pristine MOFs for electrocatalysis are their low conductivities and poor stability. Although highly conductive conjugated systems and twisted quadrilateral configurations have been developed to improve the conductivities of MOFs, which pave new ways for applications of pristine MOFs,[170–173] they are still in the exploration stage and it is very meaningful and important to construct more conductive and stable MOFs.

Secondly, although the diversity of MOFs and the weak coordination bonds make them good precursors for the preparation of catalysts with various compositions, beautiful morphologies, and specific structure, the high-cost and complicated synthesis procedure of MOFs significantly limits their large-scale application. Therefore, the development of a facile synthesis procedure and low-cost ligands to convenient construct MOFs is still urgent. And this is still very challenging nowadays. In addition, the yield of MOF derivatives is usually very low and this further increased the cost of MOF-based electrocatalysts. In this case, the composites of MOFs with other low-cost precursors may be a good choice to produce bifunctional electrocatalysts on a large scale. In addition, to maximize the utilization of MOFs, the preparation of single atom catalysts from MOFs is very attractive, especially by reducing the content of MOFs in the composites rather than using a complex post-washing method to remove the redundant metal atoms from MOF derivatives.

Thirdly, the conversion process of MOFs to their derivatives is still unclear. Nowadays, although catalysts with various compositions and morphologies can be derived from MOFs by adjusting the thermal-annealing atmosphere, temperatures, and additives. However, the decomposition of MOFs is still not very controllable and this limits the target synthesis of electrocatalysts for special applications.

Fourthly, although MOFs are good candidates for the preparation of single-atom catalysts, nowadays, the OER performance of MOF derived single-atom catalysts is still not high enough to meet the requirements of commercial applications, although the ORR performance of the catalysts is superior to that of commercial Pt/C catalysts. Therefore, it is still urgent to improve the OER performance of MOF derived single-atom catalysts in order to enhance the charging performance of Zn–air batteries. In this respect, improving the metal loadings of single-atom catalysts may be a good strategy.

Moreover, although some MOF derivatives have demonstrated to have better or competitive performances compared with those of precious metal-based catalysts, it should be pointed out that the results are obtained in the laboratory. In practical applications, ZABs face many more issues such as extreme/ever-changing temperatures and compressive stress, and the related research is very rare. In addition, the testing conditions such as the exposure of air/O_2, the loading amount of the catalysts, and the configuration of batteries have great effects on the performance of ZABs. While these conditions vary a lot in different groups, standard testing conditions should be established for better comparison of the performance of catalysts.

Overall, the development of MOF based bifunctional electrocatalysts is a significant and challenging topic in both scientific and industrial fields. Although many challenges still exist, it can be expected that the rapid development of MOF based electrocatalysts will greatly accelerate the commercialization of rechargeable ZABs.

Conflicts of interest

There are no conflicts to declare.

Acknowledgements

Notes and references

1 F. Wu, J. Maier and Y. Yu, *Chem. Soc. Rev.*, 2020, **49**, 1569–1614.
2 H. Zhang, H. Zhao, M. A. Khan, W. Zou, J. Xu, L. Zhang and J. Zhang, *J. Mater. Chem. A*, 2018, **6**, 20564–20620.
3 Y. Zhou, C. H. Wang, W. Lu and L. Dai, *Adv. Mater.*, 2020, **32**, 1902779.
4 Y. Han, G. Huang and S. Xu, *Small*, 2020, **16**, 1902841.
5 T. M. Gür, *Energy Environ. Sci.*, 2018, **11**, 2696–2767.
6 Z. Chen, A. Yu, D. Higgins, H. Li, H. Wang and Z. Chen, *Nano Lett.*, 2012, **12**, 1946–1952.
7 J. Fu, Z. P. Cano, M. G. Park, A. Yu, M. Fowler and Z. Chen, *Adv. Mater.*, 2017, **29**, 1604685.
8 Y. Hu, W. Chen, T. Lei, Y. Jiao, J. Huang, A. Hu, C. Gong, C. Yan, X. Wang and J. Xiong, *Adv. Energy Mater.*, 2020, **10**, 2000082.
9 M. Liu, N. Deng, J. Ju, L. Fan, L. Wang, Z. Li, H. Zhao, G. Yang, W. Kang, J. Yan and B. Cheng, *Adv. Funct. Mater.*, 2019, **29**, 1905467.
10 Y. Shi, Y. Chen, L. Shi, K. Wang, B. Wang, L. Li, Y. Ma, Y. Li, Z. Sun, W. Ali and S. Ding, *Small*, 2020, **16**, 2000730.
11 Y. Sun, X. Liu, Y. Jiang, J. Li, J. Ding, W. Hu and C. Zhong, *J. Mater. Chem. A*, 2019, **7**, 18183–18208.
12 W. Yu, W. Shang, P. Tan, B. Chen, Z. Wu, H. Xu, Z. Shao, M. Liu and M. Ni, *J. Mater. Chem. A*, 2019, **7**, 26744–26768.
13 J. Zhou, J. Cheng, B. Wang, H. Peng and J. Lu, *Energy Environ. Sci.*, 2020, **13**, 1933–1970.
14 Y. Guo, Y.-N. Chen, H. Cui and Z. Zhou, *Chin. J. Catal.*, 2019, **40**, 1298–1310.
15 M. Wu, G. Zhang, M. Wu, J. Prakash and S. Sun, *Energy Storage Materials*, 2019, **21**, 253–286.
16 Y. Sun, J. Wang, Q. Liu, M. Xia, Y. Tang, F. Gao, Y. Hou, J. Tse and Y. Zhao, *J. Mater. Chem. A*, 2019, **7**, 27175–27185.
17 Y. Zhu, X. Liu, S. Jin, H. Chen, W. Lee, M. Liu and Y. Chen, *J. Mater. Chem. A*, 2019, **7**, 5875–5897.
18 J. Yi, P. Liang, X. Liu, K. Wu, Y. Liu, Y. Wang, Y. Xia and J. Zhang, *Energy Environ. Sci.*, 2018, **11**, 3075–3095.

19 L. Zhang, K. Doyle-Davis and X. Sun, *Energy Environ. Sci.*, 2019, **12**, 492–517.

20 M. Liu, L. Wang, K. Zhao, S. Shi, Q. Shao, L. Zhang, X. Sun, Y. Zhao and J. Zhang, *Energy Environ. Sci.*, 2019, **12**, 2890–2923.

21 D. Liu, D. Zou, H. Zhu and J. Zhang, *Small*, 2018, **14**, 1801454.

22 B. Y. Guan, X. Y. Yu, H. B. Wu and X. W. D. Lou, *Adv. Mater.*, 2017, **29**, 1703614.

23 A. Indra, T. Song and U. Paik, *Adv. Mater.*, 2018, **30**, 1705146.

24 Y. Xue, S. Zheng, H. Xue and H. Pang, *J. Mater. Chem. A*, 2019, **7**, 7301–7327.

25 Q. Jiang, C. Zhou, H. Meng, Y. Han, X. Shi, C. Zhan and R. Zhang, *J. Mater. Chem. A*, 2020, **8**, 15271–15301.

26 L. Yang, X. Zeng, W. Wang and D. Cao, *Adv. Funct. Mater.*, 2018, **28**, 1704537.

27 X. F. Lu, B. Y. Xia, S. Q. Zang and X. W. D. Lou, *Angew. Chem., Int. Ed. Engl.*, 2020, **59**, 4634–4650.

28 G. Li, S. Zhao, Y. Zhang and Z. Tang, *Adv. Mater.*, 2018, **30**, 1800702.

29 J. Zhu, M. Xiao, Y. Zhang, Z. Jin, Z. Peng, C. Liu, S. Chen, J. Ge and W. Xing, *ACS Catal.*, 2016, **6**, 6335–6342.

30 N. Xu, Y. Zhang, M. Wang, X. Fan, T. Zhang, L. Peng, X.-D. Zhou and J. Qiao, *Nano Energy*, 2019, **65**, 104021.

31 H. F. Wang, L. Chen, H. Pang, S. Kaskel and Q. Xu, *Chem. Soc. Rev.*, 2020, **49**, 1414–1448.

32 H. Xu, S. Ci, Y. Ding, G. Wang and Z. Wen, *J. Mater. Chem. A*, 2019, **7**, 8006–8029.

33 Q. Wei, Y. Fu, G. Zhang and S. Sun, *Curr. Opin. Electrochem.*, 2017, **4**, 45–59.

34 H. Tang, M. Zheng, Q. Hu, Y. Chi, B. Xu, S. Zhang, H. Xue and H. Pang, *J. Mater. Chem. A*, 2018, **6**, 13999–14024.

35 S. Ren, X. Duan, S. Liang, M. Zhang and H. Zheng, *J. Mater. Chem. A*, 2020, **8**, 6144–6182.

36 H. Wang and J.-M. Lee, *J. Mater. Chem. A*, 2020, **8**, 10604–10624.

37 P. Prabhu, V. Jose and J.-M. Lee, *Adv. Funct. Mater.*, 2020, **30**, 1910768.

38 T. Huang, Y. Chen and J.-M. Lee, *Small*, 2017, **13**, 1702753.

39 Z. Zhao, J. Ding, R. Zhu and H. Pang, *J. Mater. Chem. A*, 2019, **7**, 15519–15540.

40 C. Han, W. Li, H.-K. Liu, S. Dou and J. Wang, *Mater. Horiz.*, 2019, **6**, 1812–1827.

41 X. Fan, J. Liu, Z. Song, X. Han, Y. Deng, C. Zhong and W. Hu, *Nano Energy*, 2019, **56**, 454–462.

42 D. Liu, B. Wang, H. Li, S. Huang, M. Liu, J. Wang, Q. Wang, J. Zhang and Y. Zhao, *Nano Energy*, 2019, **58**, 277–283.

43 H. Li, L. Ma, C. Han, Z. Wang, Z. Liu, Z. Tang and C. Zhi, *Nano Energy*, 2019, **62**, 550–587.

44 J. Kari, J. P. Olsen, K. Jensen, S. F. Badino, K. B. R. M. Krogh, K. Borch and P. Westh, *ACS Catal.*, 2018, **8**, 11966–11972.

45 K. S. Exner, *Angew. Chem., Int. Ed. Engl.*, 2020, **59**, 10236–10240.

46 Z. Wu, H. Wang, P. Xiong, G. Li, T. Qiu, W. B. Gong, F. Zhao, C. Li, Q. Li, G. Wang and F. Geng, *Nano Lett.*, 2020, **20**, 2892–2898.

47 P. Gu, M. Zheng, Q. Zhao, X. Xiao, H. Xue and H. Pang, *J. Mater. Chem. A*, 2017, **5**, 7651–7666.

48 L. Ma, S. Chen, Z. Pei, H. Li, Z. Wang, Z. Liu, Z. Tang, J. A. Zapien and C. Zhi, *ACS Nano*, 2018, **12**, 8597–8605.

49 C. Wang, H. Zhao, J. Wang, Z. Zhao, M. Cheng, X. Duan, Q. Zhang, J. Wang and J. Wang, *J. Mater. Chem. A*, 2019, **7**, 1451–1458.

50 Y. Cheng, Y. Wang, Q. Wang, Z. Liao, N. Zhang, Y. Guo and Z. Xiang, *J. Mater. Chem. A*, 2019, **7**, 9831–9836.

51 G. Li, L. Pei, Y. Wu, B. Zhu, Q. Hu, H. Yang, Q. Zhang, J. Liu and C. He, *J. Mater. Chem. A*, 2019, **7**, 11223–11233.

52 H. Yang and X. Wang, *Adv. Mater.*, 2019, **31**, 1800743.

53 S. Bhattacharyya, C. Das and T. K. Maji, *RSC Adv.*, 2018, **8**, 26728–26754.

54 D. Liu, J. Wan, G. Pang and Z. Tang, *Adv. Mater.*, 2018, **31**, 1803291.

55 Z. Liang, C. Qu, W. Guo, R. Zou and Q. Xu, *Adv. Mater.*, 2018, **30**, 1702891.

56 W. Li, S. Xue, S. Watzele, S. Hou, J. Fichtner, A. L. Semrau, L. Zhou, A. Welle, A. S. Bandarenka and R. A. Fischer, *Angew. Chem., Int. Ed.*, 2020, **59**, 5837–5843.

57 Y. Zhong, X. Xu, W. Wang and Z. Shao, *Batteries Supercaps*, 2018, **2**, 272–289.

58 D. Sheberla, L. Sun, M. A. Blood-Forsythe, S. Er, C. R. Wade, C. K. Brozek, A. Aspuru-Guzik and M. Dinca, *J. Am. Chem. Soc.*, 2014, **136**, 8859–8862.

59 S. S. Shinde, C. H. Lee, J.-Y. Jung, N. K. Wagh, S.-H. Kim, D.-H. Kim, C. Lin, S. U. Lee and J.-H. Lee, *Energy Environ. Sci.*, 2019, **12**, 727–738.

60 Y. Lian, W. Yang, C. Zhang, H. Sun, Z. Deng, W. Xu, L. Song, Z. Ouyang, Z. Wang, J. Guo and Y. Peng, *Angew. Chem., Int. Ed. Engl.*, 2020, **59**, 286–294.

61 X. Zheng, Y. Cao, D. Liu, M. Cai, J. Ding, X. Liu, J. Wang, W. Hu and C. Zhong, *ACS Appl. Mater. Interfaces*, 2019, **11**, 15662–15669.

62 Z. Xia, J. Fang, X. Zhang, L. Fan, A. J. Barlow, T. Lin, S. Wang, G. G. Wallace, G. Sun and X. Wang, *Appl. Catal., B*, 2019, **245**, 389–398.

63 S. H. Ahn, X. Yu and A. Manthiram, *Adv. Mater.*, 2017, **29**, 1606534.

64 S. H. Ahn and A. Manthiram, *Small*, 2017, **13**, 1702068.

65 Y. Qian, I. A. Khan and D. Zhao, *Small*, 2017, **13**, 1701143.

66 Y. Li, Y. Xu, W. Yang, W. Shen, H. Xue and H. Pang, *Small*, 2018, **14**, 1704435.

67 M. Y. Masoomi, A. Morsali, A. Dhakshinamoorthy and H. Garcia, *Angew. Chem., Int. Ed. Engl.*, 2019, **58**, 15188–15205.

68 Y. Peng, B. Lu and S. Chen, *Adv. Mater.*, 2018, **30**, 1801995.

69 Y. Li, M. Cui, C. Wang, Y. Chen, S. Chen, L. Gao, A. Liu, W.-N. Su and T. Ma, *Mater. Today Energy*, 2020, **17**, 100455.

70 M. Wang, H. Ji, S. Liu, H. Sun, J. Liu, C. Yan and T. Qian, *Chem. Eng. J.*, 2020, **393**, 124702.

71 J. Zhao, R. Qin and R. Liu, *Appl. Catal., B*, 2019, **256**, 117778.

72 C. Lu, R. Fang and X. Chen, *Adv. Mater.*, 2020, **32**, 1906548.

73 H. M. Barkholtz and D.-J. Liu, *Mater. Horiz.*, 2017, **4**, 20–37.

74 J. Zhang, M. Zhang, Y. Zeng, J. Chen, L. Qiu, H. Zhou, C. Sun, Y. Yu, C. Zhu and Z. Zhu, *Small*, 2019, **15**, 1900307.

75 L. Zou, C. C. Hou, Z. Liu, H. Pang and Q. Xu, *J. Am. Chem. Soc.*, 2018, **140**, 15393–15401.

76 M. Zhang, Q. Dai, H. Zheng, M. Chen and L. Dai, *Adv. Mater.*, 2018, **30**, 1705431.

77 T. Wang, Z. Kou, S. Mu, J. Liu, D. He, I. S. Amiinu, W. Meng, K. Zhou, Z. Luo, S. Chaemchuen and F. Verpoort, *Adv. Funct. Mater.*, 2018, **28**, 1705048.

78 Q. Lai, J. Zhu, Y. Zhao, Y. Liang, J. He and J. Chen, *Small*, 2017, **13**, 1700740.

79 X. Zhang, X. Han, Z. Jiang, J. Xu, L. Chen, Y. Xue, A. Nie, Z. Xie, Q. Kuang and L. Zheng, *Nano Energy*, 2020, **71**, 104547.

80 X. Han, X. Ling, Y. Wang, T. Ma, C. Zhong, W. Hu and Y. Deng, *Angew. Chem., Int. Ed. Engl.*, 2019, **58**, 5359–5364.

81 W. Zang, A. Sumboja, Y. Ma, H. Zhang, Y. Wu, S. Wu, H. Wu, Z. Liu, C. Guan, J. Wang and S. J. Pennycook, *ACS Catal.*, 2018, **8**, 8961–8969.

82 C. C. Hou, L. Zou, L. Sun, K. Zhang, Z. Liu, Y. Li, C. Li, R. Zou, J. Yu and Q. Xu, *Angew. Chem., Int. Ed. Engl.*, 2020, **59**, 7384–7389.

83 W. Wang, Y. Liu, J. Li, J. Luo, L. Fu and S. Chen, *J. Mater. Chem. A*, 2018, **6**, 14299–14306.

84 X. Zhang, J. Luo, K. Wan, D. Plessers, B. Sels, J. Song, L. Chen, T. Zhang, P. Tang, J. R. Morante, J. Arbiol and J. Fransaer, *J. Mater. Chem. A*, 2019, **7**, 1616–1628.

85 L. Chen, H.-F. Wang, C. Li and Q. Xu, *Chem. Sci.*, 2020, **11**, 5369–5403.

86 T. Liu, F. Yang, G. Cheng and W. Luo, *Small*, 2018, **14**, 1703748.

87 S. H. Ahn and A. Manthiram, *J. Mater. Chem. A*, 2019, **7**, 8641–8652.

88 Q. Shi, S. Fu, C. Zhu, J. Song, D. Du and Y. Lin, *Mater. Horiz.*, 2019, **6**, 684–702.

89 S. Abednatanzi, P. Gohari Derakhshandeh, H. Depauw, F. X. Coudert, H. Vrielinck, P. Van Der Voort and K. Leus, *Chem. Soc. Rev.*, 2019, **48**, 2535–2565.

90 X. L. Wang, L. Z. Dong, M. Qiao, Y. J. Tang, J. Liu, Y. Li, S. L. Li, J. X. Su and Y. Q. Lan, *Angew. Chem., Int. Ed. Engl.*, 2018, **57**, 9660–9664.

91 C. Wang, H. Yang, Y. Zhang and Q. Wang, *Angew. Chem., Int. Ed. Engl.*, 2019, **58**, 6099–6103.

92 X. Han, X. Ling, D. Yu, D. Xie, L. Li, S. Peng, C. Zhong, N. Zhao, Y. Deng and W. Hu, *Adv. Mater.*, 2019, **31**, 1905622.

93 C. C. Hou, L. Zou and Q. Xu, *Adv. Mater.*, 2019, **31**, 1904689.

94 J. Tan, T. Thomas, J. Liu, L. Yang, L. Pan, R. Cao, H. Shen, J. Wang, J. Liu and M. Yang, *Chem. Eng. J.*, 2020, **395**, 125151.

95 L. Chen, Y. Zhang, L. Dong, W. Yang, X. Liu, L. Long, C. Liu, S. Dong and J. Jia, *J. Mater. Chem. A*, 2020, **8**, 4369–4375.

96 Z. Wang, H. Jin, T. Meng, K. Liao, W. Meng, J. Yang, D. He, Y. Xiong and S. Mu, *Adv. Funct. Mater.*, 2018, **28**, 1802596.

97 Z. Lu, B. Wang, Y. Hu, W. Liu, Y. Zhao, R. Yang, Z. Li, J. Luo, B. Chi, Z. Jiang, M. Li, S. Mu, S. Liao, J. Zhang and X. Sun, *Angew. Chem., Int. Ed. Engl.*, 2019, **58**, 2622–2626.

98 D. Zhang, W. Chen, Z. Li, Y. Chen, L. Zheng, Y. Gong, Q. Li, R. Shen, Y. Han, W. C. Cheong, L. Gu and Y. Li, *Chem. Commun.*, 2018, **54**, 4274–4277.

99 Y. Li, H. Huang, S. Chen, X. Yu, C. Wang and T. Ma, *Nano Res.*, 2019, **12**, 2774–2780.

100 P. Tan, B. Chen, H. Xu, W. Cai, W. He and M. Ni, *Appl. Catal., B*, 2019, **241**, 104–112.

101 X. Wang, Z. Liao, Y. Fu, C. Neumann, A. Turchanin, G. Nam, E. Zschech, J. Cho, J. Zhang and X. Feng, *Energy Storage Materials*, 2020, **26**, 157–164.

102 J. Hwang, A. Ejsmont, R. Freund, J. Goscianska, B. Schmidt and S. Wuttke, *Chem. Soc. Rev.*, 2020, **49**, 3348–3422.

103 G. Saianand, A. I. Gopalan, J. C. Lee, C. I. Sathish, K. Gopalakrishnan, G. E. Unni, D. Shanbhag, V. Dasireddy, J. Yi, S. Xi, A. H. Al-Muhtaseb and A. Vinu, *Small*, 2020, **16**, 1903937.

104 X. Wang, Y. Li, T. Jin, J. Meng, L. Jiao, M. Zhu and J. Chen, *Nano Lett.*, 2017, **17**, 7989–7994.

105 R. K. Bera, H. Park and R. Ryoo, *J. Mater. Chem. A*, 2019, **7**, 9988–9996.

106 B. Zhu, D. Xia and R. Zou, *Coord. Chem. Rev.*, 2018, **376**, 430–448.

107 J. Yin, Y. Li, F. Lv, Q. Fan, Y. Q. Zhao, Q. Zhang, W. Wang, F. Cheng, P. Xi and S. Guo, *ACS Nano*, 2017, **11**, 2275–2283.

108 Y. Yin, R. M. Rioux, C. K. Erdonmez, S. Hughes, G. A. Somorjai and A. P. Alivisatos, *Science*, 2004, **304**, 711–714.

109 C. Guan, A. Sumboja, H. Wu, W. Ren, X. Liu, H. Zhang, Z. Liu, C. Cheng, S. J. Pennycook and J. Wang, *Adv. Mater.*, 2017, **29**, 1704117.

110 Z. Guo, F. Wang, Y. Xia, J. Li, A. G. Tamirat, Y. Liu, L. Wang, Y. Wang and Y. Xia, *J. Mater. Chem. A*, 2018, **6**, 1443–1453.

111 X. F. Lu, Y. Chen, S. Wang, S. Gao and X. W. D. Lou, *Adv. Mater.*, 2019, **31**, 1902339.

112 J. Yu, G. Chen, J. Sunarso, Y. Zhu, R. Ran, Z. Zhu, W. Zhou and Z. Shao, *Adv. Sci.*, 2016, **3**, 1600060.

113 Y. Jiang, Y.-P. Deng, J. Fu, D. U. Lee, R. Liang, Z. P. Cano, Y. Liu, Z. Bai, S. Hwang, L. Yang, D. Su, W. Chu and Z. Chen, *Adv. Energy Mater.*, 2018, **8**, 1702900.

114 Y. Li, C. Wang, M. Cui, S. Chen, L. Gao, A. Liu and T. Ma, *Appl. Surf. Sci.*, 2020, **509**, 145367.

115 X. Y. Yu and X. W. David Lou, *Adv. Energy Mater.*, 2018, **8**, 1701592.

116 D. Dong, Z. Wu, J. Wang, G. Fu and Y. Tang, *J. Mater. Chem. A*, 2019, **7**, 16068–16088.

117 S. Liu, X. Zhang, G. Wang, Y. Zhang and H. Zhang, *ACS Appl. Mater. Interfaces*, 2017, **9**, 34269–34278.

118 J.-Y. Zhao, R. Wang, S. Wang, Y.-R. Lv, H. Xu and S.-Q. Zang, *J. Mater. Chem. A*, 2019, **7**, 7389–7395.

119 K. Wan, J. Luo, X. Zhang, C. Zhou, J. W. Seo, P. Subramanian, J.-w. Yan and J. Fransaer, *J. Mater. Chem. A*, 2019, **7**, 19889–19897.

120 H. Yang, B. Wang, H. Li, B. Ni, K. Wang, Q. Zhang and X. Wang, *Adv. Energy Mater.*, 2018, **8**, 1801839.

121 P. Prabhu, V. Jose and J.-M. Lee, *Matter*, 2020, **2**, 526–553.

122 G. Fu and J.-M. Lee, *J. Mater. Chem. A*, 2019, **7**, 9386–9405.

123 T. Sun, S. Zhang, L. Xu, D. Wang and Y. Li, *Chem. Commun.*, 2018, **54**, 12101–12104.

124 Y. Niu, M. Xiao, J. Zhu, T. Zeng, J. Li, W. Zhang, D. Su, A. Yu and Z. Chen, *J. Mater. Chem. A*, 2020, **8**, 9177–9184.

125 Y. S. Wei, M. Zhang, M. Kitta, Z. Liu, S. Horike and Q. Xu, *J. Am. Chem. Soc.*, 2019, **141**, 7906–7916.

126 F. Meng, H. Zhong, D. Bao, J. Yan and X. Zhang, *J. Am. Chem. Soc.*, 2016, **138**, 10226–10231.

127 G. Fu, Z. Cui, Y. Chen, L. Xu, Y. Tang and J. B. Goodenough, *Nano Energy*, 2017, **39**, 77–85.

128 P. Chen, K. Xu, Z. Fang, Y. Tong, J. Wu, X. Lu, X. Peng, H. Ding, C. Wu and Y. Xie, *Angew. Chem., Int. Ed. Engl.*, 2015, **54**, 14710–14714.

129 X. Hu, Y. Min, L.-L. Ma, J.-Y. Lu, H.-C. Li, W.-J. Liu, J.-J. Chen and H.-Q. Yu, *Appl. Catal., B*, 2020, **268**, 118405.

130 H. Ge, G. Li, J. Shen, W. Ma, X. Meng and L. Xu, *Appl. Catal., B*, 2020, **275**, 119104.

131 C. Guan, A. Sumboja, W. Zang, Y. Qian, H. Zhang, X. Liu, Z. Liu, D. Zhao, S. J. Pennycook and J. Wang, *Energy Storage Materials*, 2019, **16**, 243–250.

132 S.-H. Hsu, S.-F. Hung, H.-Y. Wang, F.-X. Xiao, L. Zhang, H. Yang, H. M. Chen, J.-M. Lee and B. Liu, *Small Methods*, 2018, **2**, 1800001.

133 X. H. Yan, P. Prabhu, H. Xu, Z. Meng, T. Xue and J.-M. Lee, *Small Methods*, 2019, **4**, 1900575.

134 C. Lin, X. Li, S. S. Shinde, D.-H. Kim, X. Song, H. Zhang and J.-H. Lee, *ACS Appl. Energy Mater.*, 2019, **2**, 1747–1755.

135 Y. Lian, K. Shi, H. Yang, H. Sun, P. Qi, J. Ye, W. Wu, Z. Deng and Y. Peng, *Small*, 2020, 1907368, DOI: 10.1002/smll.201907368.

136 G. Fu, Y. Tang and J.-M. Lee, *ChemElectroChem*, 2018, **5**, 1424–1434.

137 S. S. Shinde, C. H. Lee, A. Sami, D. H. Kim, S. U. Lee and J. H. Lee, *ACS Nano*, 2017, **11**, 347–357.

138 L. Yang, J. Shui, L. Du, Y. Shao, J. Liu, L. Dai and Z. Hu, *Adv. Mater.*, 2019, **31**, 1804799.

139 R. Paul, F. Du, L. Dai, Y. Ding, Z. L. Wang, F. Wei and A. Roy, *Adv. Mater.*, 2019, **31**, 1805598.

140 C. Hu and L. Dai, *Adv. Mater.*, 2017, **29**, 1604942.

141 C. Hu and L. Dai, *Angew. Chem., Int. Ed. Engl.*, 2016, **55**, 11736–11758.

142 M. Yang, X. Hu, Z. Fang, L. Sun, Z. Yuan, S. Wang, W. Hong, X. Chen and D. Yu, *Adv. Funct. Mater.*, 2017, **27**, 1701971.

143 C. Xuan, B. Hou, W. Xia, Z. Peng, T. Shen, H. L. Xin, G. Zhang and D. Wang, *J. Mater. Chem. A*, 2018, **6**, 10731–10739.

144 Y. Qian, Z. Hu, X. Ge, S. Yang, Y. Peng, Z. Kang, Z. Liu, J. Y. Lee and D. Zhao, *Carbon*, 2017, **111**, 641–650.

145 Y. Li, Z. Yan, Q. Wang, H. Ye, M. Li, L. Zhu and X. Cao, *Electrochim. Acta*, 2018, **282**, 224–232.

146 W. Yang, X. Li, Y. Li, R. Zhu and H. Pang, *Adv. Mater.*, 2019, **31**, 1804740.

147 S. Peng, G. Jin, L. Li, K. Li, M. Srinivasan, S. Ramakrishna and J. Chen, *Chem. Soc. Rev.*, 2016, **45**, 1225–1241.

148 Z. Wang, J. Huang, J. Mao, Q. Guo, Z. Chen and Y. Lai, *J. Mater. Chem. A*, 2020, **8**, 2934–2961.

149 L. Liu, Y. Wang, F. Yan, C. Zhu, B. Geng, Y. Chen and S. l. Chou, *Small Methods*, 2019, **4**, 1900571.

150 P. Yu, L. Wang, F. Sun, Y. Xie, X. Liu, J. Ma, X. Wang, C. Tian, J. Li and H. Fu, *Adv. Mater.*, 2019, **31**, 1901666.

151 Y. Wu, W. Wang, J. Ming, M. Li, L. Xie, X. He, J. Wang, S. Liang and Y. Wu, *Adv. Funct. Mater.*, 2019, **29**, 1805978.

152 S. Wei, L. Ma, K. E. Hendrickson, Z. Tu and L. A. Archer, *J. Am. Chem. Soc.*, 2015, **137**, 12143–12152.

153 Y. Chen, W. Zhang, Z. Zhu, L. Zhang, J. Yang, H. Chen, B. Zheng, S. Li, W. Zhang, J. Wu and F. Huo, *J. Mater. Chem. A*, 2020, **8**, 7184–7191.

154 Y. Zhao, Q. Lai, J. Zhu, J. Zhong, Z. Tang, Y. Luo and Y. Liang, *Small*, 2018, **14**, 1704207.

155 W. Zhang, X. Yao, S. Zhou, X. Li, L. Li, Z. Yu and L. Gu, *Small*, 2018, **14**, 1800423.

156 J. Di, J. Guo, N. Wang and G. Ma, *ACS Sustainable Chem. Eng.*, 2019, **7**, 7716–7727.

157 D. Ji, L. Fan, L. Li, N. Mao, X. Qin, S. Peng and S. Ramakrishna, *Carbon*, 2019, **142**, 379–387.

158 Q. Zhou, Z. Zhang, J. Cai, B. Liu, Y. Zhang, X. Gong, X. Sui, A. Yu, L. Zhao, Z. Wang and Z. Chen, *Nano Energy*, 2020, **71**, 104592.

159 Y.-N. Chen, Y. Guo, H. Cui, Z. Xie, X. Zhang, J. Wei and Z. Zhou, *J. Mater. Chem. A*, 2018, **6**, 9716–9722.

160 H. Sun, Q. Li, Y. Lian, C. Zhang, P. Qi, Q. Mu, H. Jin, B. Zhang, M. Chen, Z. Deng and Y. Peng, *Appl. Catal., B*, 2020, **263**, 118139.

161 Y. Xu, P. Deng, G. Chen, J. Chen, Y. Yan, K. Qi, H. Liu and B. Y. Xia, *Adv. Funct. Mater.*, 2019, **30**, 1906081.

162 L. Ma, S. Chen, Z. Pei, Y. Huang, G. Liang, F. Mo, Q. Yang, J. Su, Y. Gao, J. A. Zapien and C. Zhi, *ACS Nano*, 2018, **12**, 1949–1958.

163 H. Zou, G. Li, L. Duan, Z. Kou and J. Wang, *Appl. Catal., B*, 2019, **259**, 118100.

164 S. Liu, M. Wang, X. Sun, N. Xu, J. Liu, Y. Wang, T. Qian and C. Yan, *Adv. Mater.*, 2018, **30**, 1704898.

165 X. Xu, Z. Xia, X. Zhang, R. Sun, X. Sun, H. Li, C. Wu, J. Wang, S. Wang and G. Sun, *Appl. Catal., B*, 2019, **259**, 118042.

166 Y. Xu, Z. Huang, B. Wang, Z. Liang, C. Zhang, Y. Wang, W. Zhang, H. Zheng and R. Cao, *Chem. Commun.*, 2019, **55**, 14805–14808.

167 C. Zhang, H. Yang, D. Zhong, Y. Xu, Y. Wang, Q. Yuan, Z. Liang, B. Wang, W. Zhang, H. Zheng, T. Cheng and R. Cao, *J. Mater. Chem. A*, 2020, **8**, 9536–9544.

168 S. Liu, Z. Wang, S. Zhou, F. Yu, M. Yu, C. Y. Chiang, W. Zhou, J. Zhao and J. Qiu, *Adv. Mater.*, 2017, **29**, 1700874.

169 D. Ren, J. Ying, M. Xiao, Y. P. Deng, J. Ou, J. Zhu, G. Liu, Y. Pei, S. Li, A. M. Jauhar, H. Jin, S. Wang, D. Su, A. Yu and Z. Chen, *Adv. Funct. Mater.*, 2019, **30**, 1908167.

170 Y. Zhu and Z. Tang, *Matter*, 2020, **2**, 798–800.

171 H. Huang, Y. Zhao, Y. Bai, F. Li, Y. Zhang and Y. Chen, *Adv. Sci.*, 2020, **7**, 2000012.

172 T. S. Wang, X. Liu, X. Zhao, P. He, C. W. Nan and L. Z. Fan, *Adv. Funct. Mater.*, 2020, **30**, 2000786.

173 J. Su, W. He, X.-M. Li, L. Sun, H.-Y. Wang, Y.-Q. Lan, M. Ding and J.-L. Zuo, *Matter*, 2020, **2**, 711–722.